SYNGAP1 heterozygosity disrupts sensory processing by reducing touch-related activity within somatosensory cortex circuits

Sheldon D. Michaelson[1,7], Emin D. Ozkan[1,7], Massimiliano Aceti[1,6], Sabyasachi Maity[1], Nerea Llamosas[1], Monica Weldon[2], Elisa Mizrachi[1], Thomas Vaissiere[1], Michael A. Gaffield[3], Jason M. Christie[3], J. Lloyd Holder Jr.[4], Courtney A. Miller[1,5] and Gavin Rumbaugh[1,5]*

In addition to cognitive impairments, neurodevelopmental disorders often result in sensory processing deficits. However, the biological mechanisms that underlie impaired sensory processing associated with neurodevelopmental disorders are generally understudied and poorly understood. We found that SYNGAP1 haploinsufficiency in humans, which causes a sporadic neurodevelopmental disorder defined by cognitive impairment, autistic features, and epilepsy, also leads to deficits in tactile-related sensory processing. In vivo neurophysiological analysis in Syngap1 mouse models revealed that upper-lamina neurons in somatosensory cortex weakly encode information related to touch. This was caused by reduced synaptic connectivity and impaired intrinsic excitability within upper-lamina somatosensory cortex neurons. These results were unexpected, given that Syngap1 heterozygosity is known to cause circuit hyperexcitability in brain areas more directly linked to cognitive functions. Thus, Syngap1 heterozygosity causes a range of circuit-specific pathologies, including reduced activity within cortical neurons required for touch processing, which may contribute to sensory phenotypes observed in patients.

N eurodevelopmental disorders (NDD) often result in poor cognitive functioning and impaired behavioral adaptations. While the precise neurobiological and neurophysiological mechanisms that underlie these impairments remain unknown, it is generally understood that they are a consequence of impaired connectivity and processing within neuronal networks[1–4]. However, it remains unclear what brain areas are disrupted and how neural processing within affected areas contributes to cognitive and behavioral impairments. Therefore, it is critical to identify dysfunctional brain areas that contribute to NDD-relevant phenotypes and to then define the circuit-based mechanisms that contribute to them.

Sensory-processing impairments are nearly ubiquitous in NDDs, and we have a growing appreciation for their central role in behavioral and cognitive deficits associated with these[5] and related[6] disorders. Mechanistic studies in NDD animal models have traditionally focused on the circuits and synapses located in brain regions associated with cognitive functions[4]. These studies have demonstrated that NDD risk genes impair synapse properties, such as plasticity and excitatory–inhibitory ratios, which are believed to underlie impaired cognitive functions and common comorbidities, such as epilepsy. However, less attention has been paid to the mechanisms contributing to sensory processing deficits, particularly at the level of primary cortical circuits, which integrate ascending sensory information with top-down modulatory signals from higher cortical areas[7]. Indeed, higher forms of cognition require information regarding the external environment. Primary sensory cortical areas decode stimulus features[8] and facilitate the construction of complex internal representations of the external world[9]. In this context, disrupted lower-level sensory processing in NDDs could contribute to generalized cognitive and behavioral impairments reported in people with these disorders. At present, it remains unclear how impairments in sensory processing contribute to complex cognitive and behavioral phenotypes common to people with NDDs. This stems from a relative lack of mechanistic, systems-based studies investigating how highly penetrant NDD risk factors directly impact the function of circuits that process sensory information.

A tractable entry point for such mechanistic studies is to perform in-depth biological investigations of highly penetrant rare variants known to cause well-understood childhood NDDs[10,11]. The *SYNGAP1* gene is frequently mutated in intellectual disability (ID) associated with classically undefined global developmental delay[12–15] and is a major risk factor for autism spectrum disorders[16,17]. De novo nonsense variants in *SYNGAP1* resulting in haploinsufficiency lead to a genetically defined form of ID (MRD5; OMIM #603384) that may explain up to 1% of these cases[18,19]. MRD5 patients suffer from cognitive impairments, such as absent or poor language acquisition, and very low nonverbal IQ[19,20]. *SYNGAP1* is also a risk factor for epileptic encephalopathies[21,22], and most MRD5 patients have comorbid epilepsy[18–20]. Currently, the impact of *SYNGAP1*/*Syngap1* pathogenicity on sensory functions is unknown, but this knowledge is necessary for a deeper understanding of the complex phenotypes observed in this genetically defined NDD.

We report altered sensory functions in a *SYNGAP1* patient population, including behaviors related to abnormal tactile processing. Studies in a series of construct-valid mouse models of *SYNGAP1* haploinsufficiency revealed severe impairments in somatosensory

cortex (SSC) circuit structure and function. *Syngap1* heterozygosity resulted in reduced connectivity and hypoexcitability within upper-lamina SSC glutamatergic neurons, resulting in reduced touch-related activity within these circuits. These results were unexpected, as they were distinct from mechanisms described in associational brain areas more directly linked to cognitive function, such as increased synaptic excitability of circuits in the hippocampus[23] and prefrontal cortex[24]. Thus, pathogenicity of *Syngap1* causes a range of circuit-specific pathologies. We propose a generalizable scheme in which interactions among region-specific circuit pathologies due to causally linked NDD risk variants drive complex cognitive and behavioral phenotypes observed in people with NDDs.

Results

SYNGAP1 heterozygosity in humans leads to touch-related sensory processing defects.

To explore how sensory function is impacted by *SYNGAP1* pathogenesis, we mined data from a *SYNGAP1* patient registry that is a component of an ongoing retrospective MRD5 natural history study. Registries are essential tools to discover common phenotypes in patients with rare genetic disorders[25]. This registry contains a searchable database with anonymized medical records, including genetic reports and detailed medical histories for *SYNGAP1* patients (https://syngap1registry.iamrare.org). Forty-eight unique registry entries contained a comprehensive medical history and completed questionnaire focusing on sensory function. Of these, 45 exhibited features consistent with sensory processing impairments (Supplementary Table 1). Twenty of these entries were supported by detailed narrative accounts describing abnormal responses to tactile stimuli, which included blunted responses to painful touch-related stimuli and/or tactile-seeking or tactile-aversive behaviors (Supplementary Table 2). Genetic reports were available for 17 of the 20. Fourteen of the 17 reports identified the *SYNGAP1* variant as clearly pathogenic (that is, caused *SYNGAP1* heterozygosity) and the cause of their developmental disorder (Supplementary Table 2). The other three reports included variants of undetermined but potential clinical significance that require further biological validation, such as predicted splice alterations or missense mutations. Data from these detailed patient entries indicate that disrupting expression or function of *SYNGAP1* in humans can lead to tactile-related sensory impairments in addition to cognitive impairment and seizure.

Syngap1 heterozygosity in mice causes touch-related deficits in cortical circuit activation.

We next used mouse models to understand the biological mechanisms of sensory processing deficits associated with human *SYNGAP1* heterozygosity. The barrel field of the SSC processes touch-related sensory information generated by movements and angular deflections of whiskers[8]. Computations here promote touch-related sensory perception and object localization and facilitate the creation of spatial maps of the environment[8,9], all processes that facilitate higher-order cognitive functions. First, we mapped cortical receptive fields of whiskers in anesthetized *Syngap1* mice by measuring intrinsic optical signals (IOS) generated by whisker deflections (Fig. 1a,b). The amplitude of cortical IOS elicited from C2 and β whisker deflections, as measured by the peak IOS response (Fig. 1c–e) and the area of the absolute value of the thresholded signal (Fig. 1g), was significantly reduced in both whisker-related receptive fields tested in *Syngap1*-heterozygous mice (Het mice). This result was unexpected, given that *Syngap1* pathogenicity has routinely been linked to circuit hyperexcitability[18,21,23,24,26,27]. However, both the distance between the two fields (Fig. 1f) and their size, as measured by the relative area of the IOS signal (Fig. 1h), did not differ from those of wild-type (WT) mice. Reduced cortical activation in *Syngap1* mouse barrel SSC was confirmed by widefield, low-resolution imaging of barrel cortex in Thy1-GCaMP6s mice (GP4.3 line[28]) crossed to *Syngap1* mice

under anesthesia. In these studies, *Syngap1* Het mice also exhibited reduced amplitudes of SSC whisker-evoked responses compared to controls (Supplementary Fig. 1a–l). Moreover, alterations in whisker-evoked signals in SSC were stimulus-dependent, with larger effect sizes occurring in response to stronger stimuli. These findings indicate that receptive field topology is generally unaltered in *Syngap1* mice, but that cortical activation driven by whisker input is impaired by *Syngap1* heterozygosity.

To better understand altered SSC functional activation in *Syngap1* mice, we measured spike-like suprathreshold somatic calcium events in layer (L) 2/3 SSC neurons. These SSC neurons were chosen because they are readily accessible by two-photon imaging and known to integrate bottom-up sensory signals originating in the periphery with information arriving from higher cortical areas[7]. Somatic calcium events were measured through in vivo two-photon imaging of GCaMP6 dynamics in awake, headfixed *Syngap1* mice crossed to the GP4.3 line (Fig. 2a–c). These studies were performed in awake animals because anesthesia disrupts neuronal activity and can have complex effects in mouse models of NDD risk genes[29]. We mapped the cortical receptive field of a single whisker and then loaded this whisker into a small plastic holder. Mice spontaneously whisked during the imaging trials, which resulted in the whisker contacting the sides of the holder (Supplementary Video 1). Thus, recorded activity during these trials was comprised of ongoing, spontaneous activity of unknown origins and activity generated by whisker movements and/or touch. Neurons in L2/3 SSC generally appeared less active in Het mice than in WT mice (Fig. 2b). Further analysis revealed that while the size of the responsive population was not affected in *Syngap1* Het mice (Fig. 2d), neurons that were active during the imaging session had significantly smaller (Fig. 2e) and less numerous (Fig. 2f) events compared to WT neurons. After these imaging sessions, we injected the whisker pad with onabotulinumtoxinA (Botox) to paralyze whisker movements (Supplementary Video 2) and reimaged L2/3 cellular activity in the same animal population 1 week later. Botox had no effect on the size of the responsive population (Fig. 2d). Botox also had no effect on event amplitudes within genotypes, and the difference between genotypes remained even in the presence of whisker paralysis (Fig. 2e). However, Botox had a clear impact on the number of detected events in this experiment. For example, in WT animals, whisker paralysis shifted the cumulative fraction of neuronal activity counts to the left (Fig. 2f). We reasoned that the shift in the 'event number' curves after Botox injection reflected the contribution of whisker movements and/or touch to activity within this population. In contrast, Botox did not shift the activity of Het neurons (Fig. 2f). Neurons from Botox+ Het mice appeared to have activity counts that were identical to those of neurons in Botox− Het mice, indicating that whisker movements and/or touch resulted in less activity than it did in WT mice. Indeed, the Het activity curves were superimposed onto those of Botox-treated WT neurons. While these shifts in spike-like activity may seem subtle, it is known that spiking within a small population of cortical neurons is sufficient to drive a behavioral response[30]. Thus, it is reasonable that a small yet highly consequential change in the number of detected spike-like events generated in Het mice, especially spike-like activity linked to touch, is likely to be behaviorally meaningful to these animals.

The lack of Botox effects on neuronal activity in Het mice was supported by a cluster analysis of activity counts from neurons imaged in all four conditions. In each condition, active neurons were clustered into low-, medium-, and high-activity populations[31] based on the number of spikes during the recording session (Supplementary Fig. 2a). This analysis showed an overall effect on how the neurons clustered across the four groups (Supplementary Fig. 2b) and revealed a difference in each of the three activity clusters when comparing the four experimental groups (Supplementary Fig. 2c). However, post hoc analyses comparing the four groups to
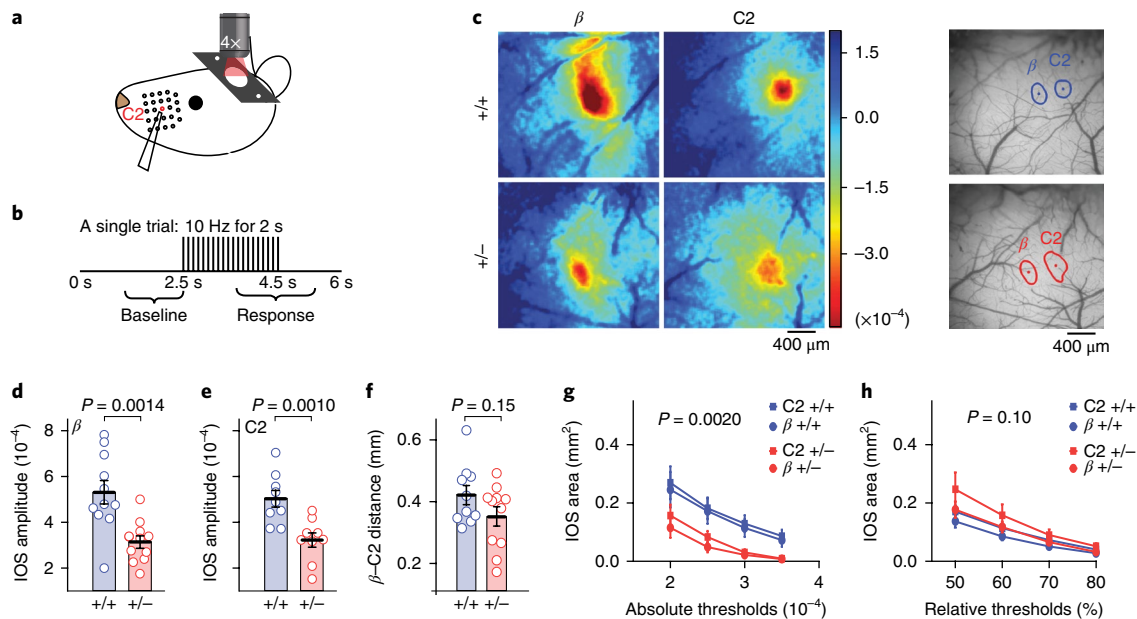
Fig. 1 | Reduced sensory-evoked brain activity in *Syngap1* SSC. a,b, Stimulus framework used during IOS imaging. **c,** Example IOS signals from 1 animal per genotype (WT, +/+; Het, +/−) obtained for β and C2 whiskers. **d–f,** Scatter plots showing reduced IOS amplitudes in (**d**) β and (**e**) C2 whisker fields, but (**f**) normal interbarrel distance in adult *Syngap1* mutants (unpaired two-sided *t* tests; β amplitude: $t_{20} = 3.76$, $P = 0.0014$, $n = 11$ WT, $n = 11$ Het mice; for C2 amplitude: $t_{16} = 3.70$, $P = 0.001$, $n = 9$ WT, $n = 9$ Het mice; for interbarrel distance: $t_{19} = 1.49$, $P = 0.15$, $n = 10$ WT, $n = 11$ Het mice). Open circles represent animal means; black lines indicate population means and error bars indicate s.e.m. **g,h,** Quantification of the area responding to β or C2 whisker stimulation according to (**g**) absolute or (**h**) relative thresholding methods (two-way repeated-measures (RM) ANOVA for absolute area, genotype: $F_{1,36} = 11.18$, $P = 0.002$; genotype × threshold: $F_{3,108} = 1.74$, $P = 0.163$; two-way RM-ANOVA for relative area, genotype: $F_{1,36} = 2.8$, $P = 0.1$; genotype × threshold: $F_{3,108} = 2.92$, $P = 0.037$; $n = 20$ WT, $n = 20$ Het IOS imaging sessions from different whiskers). Closed circles and squares represent population means and error bars indicate s.e.m. Data in this figure were acquired from two independent cohorts of animals that were pooled together.

each other revealed that all three activity clusters from the Botox⁻ WT mice were different from the corresponding clusters from all other groups (Supplementary Fig. 2d). The difference arose from the larger numbers of neurons present in the high- and medium-activity clusters and smaller number of neurons in the low-activity cluster in the Botox⁻ WT compared to the other three groups, further supporting the idea that Botox reduced activity within WT, but not Het, SSC circuits. Reduced activity generated from free whisking and/or touch in *Syngap1* mice could be caused by impaired whisking behaviors in these animals, such as a decrease in total time whisking. Unexpectedly, *Syngap1* Het mice spent more time freely whisking compared to WT mice (Fig. 2g). Taken together, these findings indicate that activity driven by free whisker movement and/or whisker curvature driven by touch was poorly encoded by L2/3 SSC neurons in *Syngap1* mice.

To further investigate the possibility that *Syngap1* heterozygosity impacts SSC cellular activity generated by whisker curvature, we measured cellular response properties in SSC L2/3 neurons evoked by piezo-driven, passive whisker deflections in awake, headfixed Syngap1-GP4.3 mice. We observed an effect of genotype on several measures of stimulus-evoked neuronal activity (Fig. 3a–h), each consistent with reduced activation of L2/3 SSC neurons. A mild stimulus (5 pulses, 5 Hz) resulted in a smaller responsive population in Het mice (Fig. 3c), but no change in the sizes of individual responses or the probability that a cell would respond to the stimulus (Fig. 3d,e). However, a stronger stimulus often used in single whisker-stimulation-detection experiments, such as 60 pulses at 40 Hz, resulted in a smaller active population (Fig. 3f), a reduced amplitude of sensory-evoked events (Fig. 3g), and reduced response probability of responsive cells (Fig. 3h) in Het mice. Active whisking could theoretically disrupt the quality of investigator-controlled passive deflections in a genotype-specific manner through degradation

of precise whisker control. To control for this possibility, we performed stimulus-evoked trials in the same cohort of animals following injection of Botox into the whisker pad. After whisker paralysis, we continued to observe reduced cellular sensory responsiveness arising from passive whisker deflections in Het mice (Fig. 3i–n). For both stimuli, we observed a reduction in the response probably of the whisker-responsive population in Het mice (Fig. 3k,n). However, other cellular response phenotypes were less pronounced after whisker paralysis, including the absence of change in the event amplitude of the responsive population (Fig. 3j,m) and the size of the responsive population (Fig. 3i,l). Together, these data demonstrate that whisker bending through passive deflections resulted in reduced activity within SSC of *Syngap1* mice.

We next asked whether cortex-specific mechanisms contribute to the reduced SSC activity observed in *Syngap1* Het mice by restricting *Syngap1* heterozygosity to forebrain glutamatergic neurons. *Syngap1* conditional knockout (cKO) mice[23] were crossed to a series of Cre drivers that express the recombinase in different subclasses of forebrain neurons, and then we injected these animals with an adeno-associated viral vector that drives GCaMP6s expression. *Syngap1*-cKO mice were first crossed to an Emx1-Cre driver[32], in which Cre expression is restricted to forebrain glutamatergic neurons and glia, and we performed in vivo two-photon imaging of calcium dynamics in L2/3 SSC neurons (Fig. 4a,b). We have previously confirmed that this cross results in reduced SynGAP expression within forebrain excitatory neurons[24]. Two-photon calcium activity measurements were obtained from mice anesthetized to prevent spontaneous whisking, allowing precise control of stimulus conditions. Restricting *Syngap1* pathogenicity to this cellular population did not change the size of the active cell population (Fig. 4c), but it did disrupt the amplitude and neuronal response probability of sensory-evoked responses (Fig. 4d,e). These
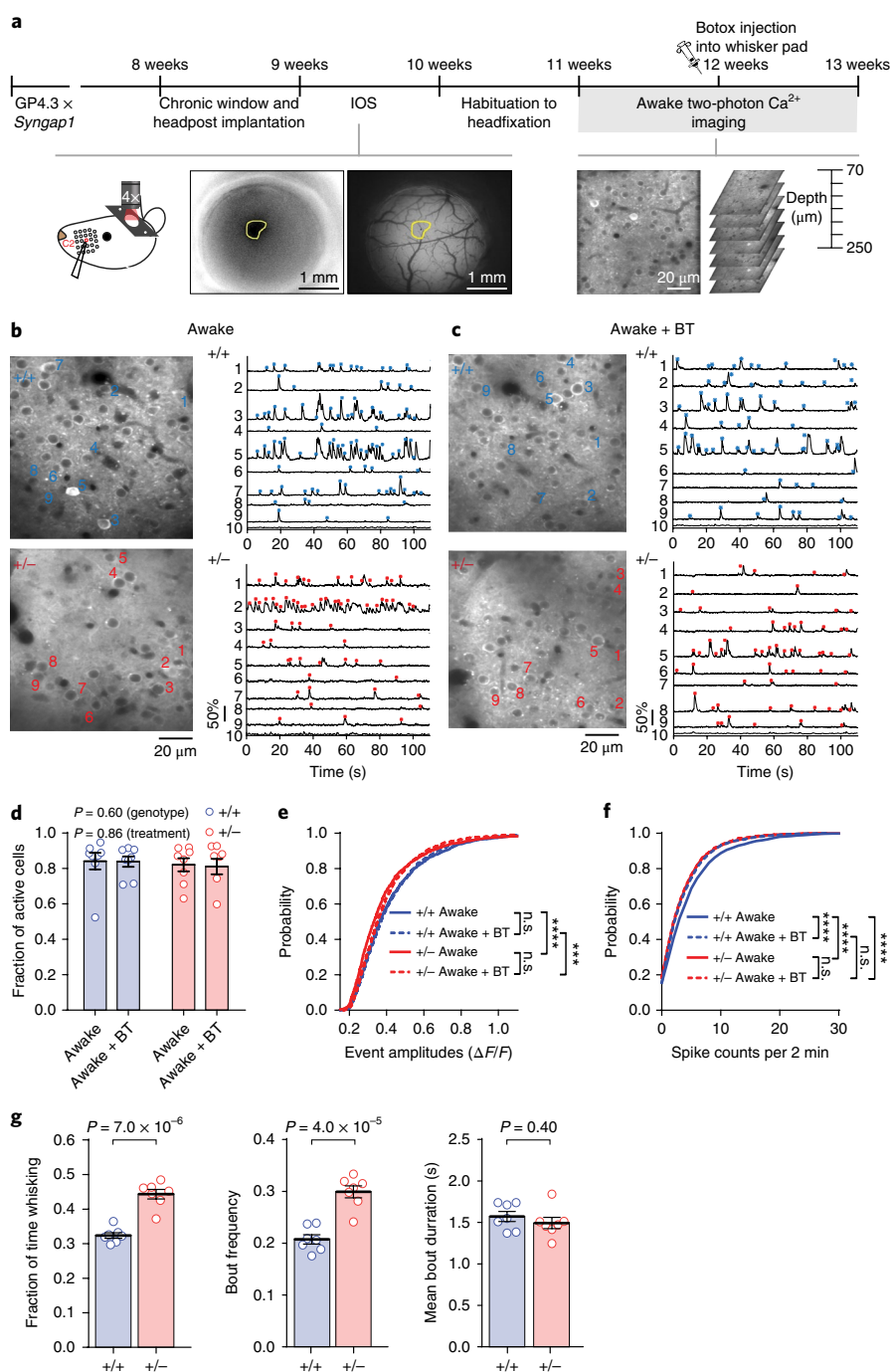
Fig. 2 | Reduced ongoing and whisker-generated activity in SSC L2/3 neurons from awake *Syngap1* mice. a, Experimental setup for awake, in vivo two-photon calcium imaging in *Syngap1* mice crossed with Thy1-Gcamp6s4.3 mice, with and without Botox (BT) injection. **b,c**, Representative in vivo two-photon microscopy images (left) and ΔF/F traces (right) of spontaneous activity in 9 (1–9) neurons of L2/3 SSC of WT and Het *Syngap1*×Thy1-GCaMP6s4.3 mice, (**b**) without and (**c**) with Botox. Region of interest (ROI) 10 is the neuropil signal. Asterisks indicate detected calcium events (blue, WT mice; red, Het mice). **d–f**, Cellular sensory properties from awake WT and Het mice without and with Botox injection. (**d**) Scatter plot showing fraction of spontaneously active cells in WT and Het mice (two-way RM-ANOVA, genotype: $F_{1,14} = 0.29$, $P = 0.60$; treatment: $F_{1,14} = 0.034$, $P = 0.86$; interaction: $F_{1,14} = 0.012$, $P = 0.92$; $n = 8$ WT mice, $n = 8$ Het mice). (**e–f**) Cumulative probability plots of (**e**) ΔF/F amplitudes (Kolmogorov–Smirnov (KS) tests: WT Botox⁻ vs. Het Botox⁻, $P = 3.38 \times 10^{-7}$; WT Botox⁺ vs. Het Botox⁺, $P = 0.0002$; WT Botox⁻ vs. WT Botox⁺, $P = 0.67$; Het Botox⁻ vs. Het Botox⁺, $P = 0.078$; WT mice: $n = 1{,}622$ Botox⁻ neurons, 1,827 Botox⁺ neurons; Het mice: $n = 1{,}667$ Botox⁻ neurons, 1,600 Botox⁺ neurons) and (**f**) spike counts (KS tests: WT Botox⁻ vs. Het Botox⁻, $P = 1.82 \times 10^{-7}$; WT Botox⁻ vs. WT Botox⁺, $P = 7.99 \times 10^{-6}$; WT Botox⁻ vs. Het Botox⁺, $P = 2.87 \times 10^{-8}$; Het Botox⁻ vs. Het Botox⁺, $P = 0.99$; WT Botox⁺ vs. Het Botox⁺, $P = 0.24$). (**g**) Whisking behavior in headfixed *Syngap1* mice (unpaired *t* tests; fraction of time whisking: $t_{12} = 7.493$, $P = 7.0 \times 10^{-6}$; $n = 7$ WT mice, 7 Het mice; bout frequency: $t_{12} = 6.298$, $P = 4.0 \times 10^{-5}$; $n = 7$ WT mice, 7 Het mice; mean bout duration: $t_{12} = 0.8714$, $P = 0.40$; $n = 7$ WT mice, 7 Het mice). Data were pooled from two independent cohorts of animals and thus obtained from 2,169 neurons in 56 imaging planes from 8 WT mice and 1,971 neurons in 55 imaging planes from 8 Het mice. In scatter plots, open circles are animal means, black lines indicate population means, and error bars indicate s.e.m. ***$P < 0.001$, ****$P < 0.0001$ for cumulative probability plots; n.s., not significant. All statistical tests were two-sided.

Fig. 3 | Reduced whisker responsiveness of SSC neurons in behaving *Syngap1* mice. a,b, Representative in vivo two-photon microscopy images (**a**) and representative ΔF/F traces (**b**) of 9 (1–9) neurons in WT and Het (Botox⁻) mice in response to 5 passive whisker deflections at 5 Hz. Gray vertical lines indicate the timing of whisker stimuli. Green asterisks indicate calcium events within the response detection window. Red asterisks show spontaneous calcium events. ROI 10 is the neuropil signal. **c–h,** Cellular sensory properties from awake animals in response to (**c–e**) 5 pulses at 5 Hz and (**f–h**) 60 pulses at 40 Hz whisker stimulation. (**c**) Scatter plot showing fraction of responding cells in WT and Het mice (unpaired *t* test; $t_{14} = 2.48$, $P = 0.026$; $n = 8$ WT mice, 8 Het mice). (**d,e**) Cumulative probability and scatter plots (insets) of (**d**) ΔF/F amplitudes (KS test, $P = 0.13$; $n = 406$ WT neurons, $n = 330$ Het neurons) and (**e**) response probabilities (KS test, $P = 0.23$) in responding neurons. (**f**) Scatter plot depicting fraction of responding cells in WT and Het mice (unpaired *t* test $t_{14} = 3.07$, $P = 0.0084$; $n = 8$ WT mice, 8 Het mice). (**g,h**) Cumulative probability and scatter plots (insets) of (**g**) ΔF/F amplitudes (KS test, $P = 0.00050$; $n = 467$ WT neurons, 368 Het neurons) and (**h**) response probabilities (KS test, $P = 0.0059$) in responding neurons. **i–n,** Cellular sensory properties from awake animals following Botox injection in response to (**i–k**) 5 pulses at 5 Hz and (**l–n**) 60 pulses at 40 Hz whisker stimulation. (**i**) Scatter plot depicting fraction of responding cells in WT and Het mice (unpaired *t* test, $t_{14} = 0.35$, $P = 0.73$; $n = 8$ WT mice, 8 Het mice). (**j,k**) Cumulative probability and scatter plots (insets) of (**j**) ΔF/F amplitudes (KS test, $P = 0.32$; $n = 413$ WT neurons, 416 Het neurons) and (**k**) response probabilities (KS test, $P = 0.0061$) in responding neurons. (**l**) Scatter plot showing fraction of responding cells in WT and Het mice (unpaired *t* test, $t_{14} = 0.11$, $P = 0.92$; $n = 8$ WT mice, 8 Het mice). (**m,n**) Cumulative probability and scatter plots (insets) of (**m**) ΔF/F amplitudes (KS test, $P = 0.39$; $n = 481$ WT neurons, 445 Het neurons) and (**n**) response probabilities (KS test, $P = 0.010$) in responding neurons. Data in **c–h** obtained from 1,921 neurons in 54 imaging planes from 8 WT mice and 2,044 neurons in 54 imaging planes from 8 Het mice. Data in **i–n** were obtained from 2,169 neurons in 56 imaging planes from 8 WT mice and 1,971 neurons in 55 imaging planes from 8 Het mice. Data were pooled from two independent cohorts of animals. In scatter plots, open circles are animal means, closed circles are individual cells, black lines indicate population means, and error bars indicate s.e.m. All statistical tests were two-sided.

data were largely consistent with findings in conventional non-whisking awake *Syngap1* animals (that is, Botox-injected animals shown in Fig. 3i–k), although the effects here were stronger than in this prior experiment. The stronger phenotype in this experiment could be due to the method (virally injected GCaMP6s versus GP4.3 transgene expression), brain state (anesthesia versus awake), the cell types expressing *Syngap1* heterozygosity (EMX1⁺-restricted population versus no restrictions), or some combination of these factors. Nevertheless, reduced sensory responsiveness of L2/3 SSC neurons in *Syngap1* mice is a reproducible phenotype and implicates *Syngap1*-mediated pathology directly in forebrain neurons.

Syngap1 cKOs were next crossed to Cre driver lines that induce recombination in non-overlapping EMX1⁺ subpopulations and imaged under the same conditions as in the EMX1 experiment. Restricting *Syngap1* heterozygosity to upper-lamina cortical neurons in Cux2-Cre^ERT2 mice, an extensively validated Cre driver line selective for upper-lamina neurons in neocortex[33] (Supplementary Fig. 3a,b), did not impact the size of the responsive population or neuronal response probability (Fig. 4f,h). However, it caused a weak, but significant, reduction in amplitude of evoked responses (Fig. 4g). Next, we restricted *Syngap1* heterozygosity to L5 glutamatergic neurons using the validated Rbp4-Cre driver line[33] (Supplementary Fig. 3c,d) and imaged calcium responses in L2/3 barrel cortex neurons. Disrupting *Syngap1* only in these neurons did not alter any of the standard measures of neuron responsiveness to sensory
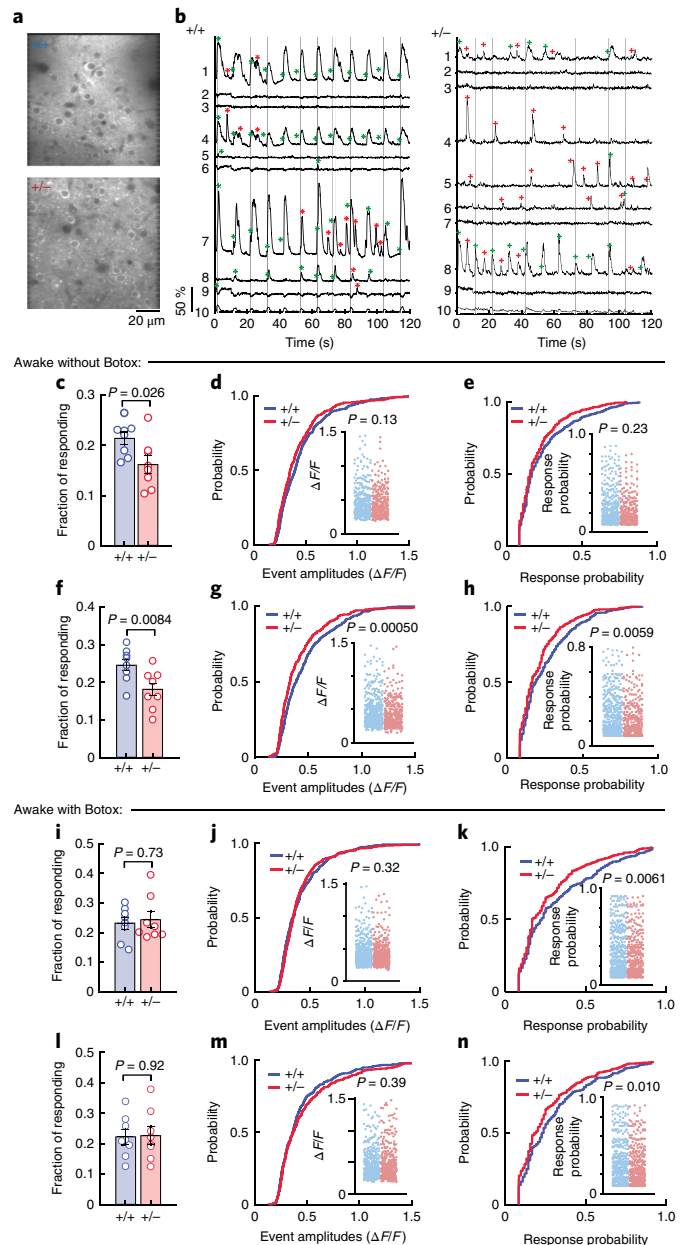
stimulation (Fig. 4i–k). While we have measured reduced whisker-evoked activity within Layer 2/3 neurons in both conventional and EMX1-Syngap1 Het mice, the primary cellular origins of how *Syngap1* heterozygosity leads to effects on Layer 2/3 neurons are complex and not necessarily autonomous to only these neurons. The inability to fully recapitulate the sensory-responsive phenotypes of EMX1-Cre models in Cux2-Cre or RBP4-Cre models indicates that *Syngap1* pathogenicity directly alters the function of multiple EMX1⁺ populations that converge to drive the SSC cellular responsiveness phenotypes observed in conventional *Syngap1* Het mice.

Reduced sensory responsiveness could be caused by decreased excitation or increased inhibition on, or in, upper-lamina L2/3 SSC neurons. To test the latter possibility, we crossed *Syngap1* mice with Gad2-T2A-NLS-mCherry mice[7] and injected them with an adeno-associated viral vector that drives GCaMP6s expression in inhibitory and excitatory neurons (Fig. 5a,b). Under anesthesia, mCherry⁻ (excitatory) neurons exhibited a substantial reduction in neuronal activation in response to passive whisker stimulation (Fig. 5c–e). The reduced activation of neurons was most apparent in the whisker-responsive population (Fig. 5e). Among this
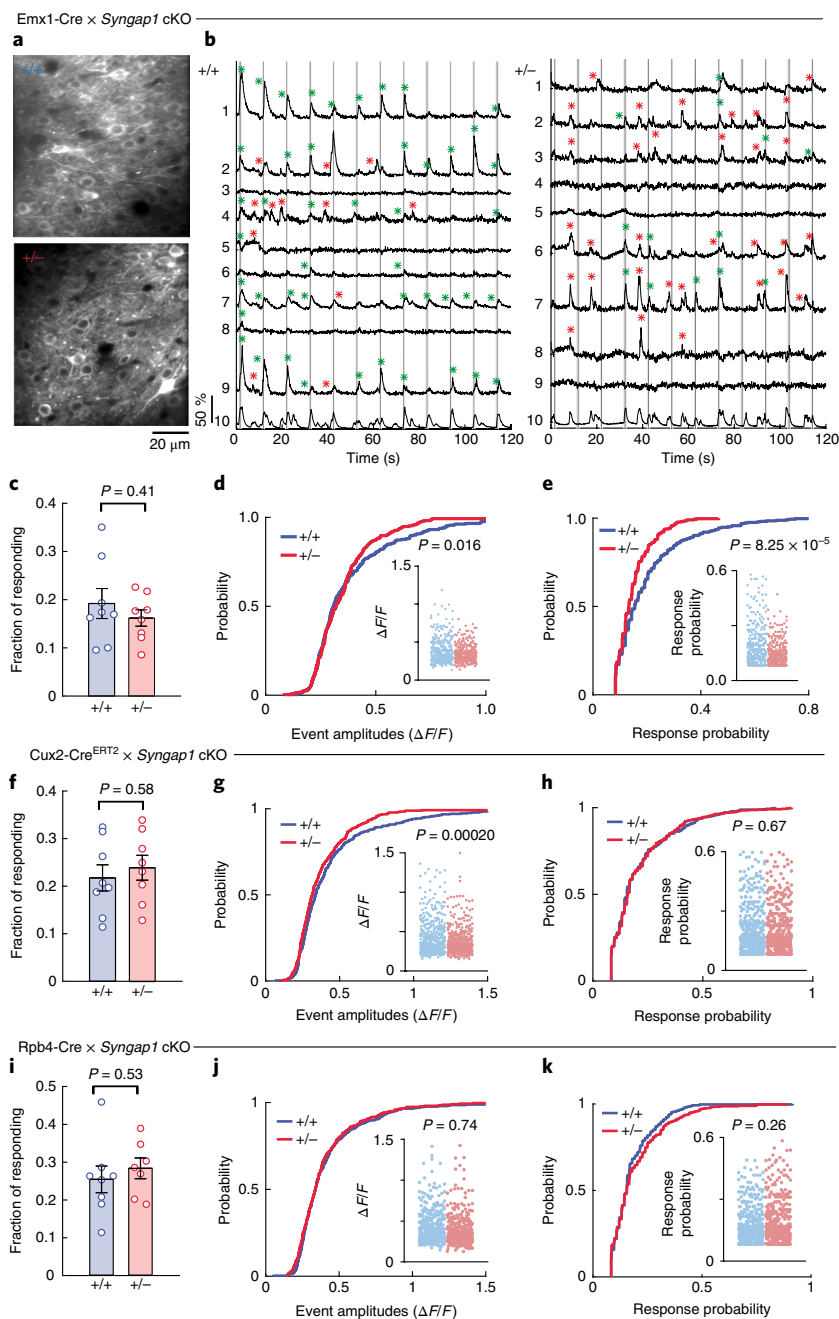
Fig. 4 | Reduced sensory responsiveness of L2/3 SSC neurons in *Syngap1* mice is cortex-specific. a, Representative in vivo two-photon microscopy images of L2/3 SSC of WT and Het Emx1-Cre×*Syngap1* cKO mice. **b,** Representative $\Delta F/F$ traces of 9 (1–9) neurons in WT and Het mice in response to 5 passive whisker deflections at 5 Hz (from **a**). Gray vertical lines indicate the timing of whisker stimulus. Green asterisks indicate calcium events within the response detection window. Red asterisks show spontaneous calcium events. ROI 10 is the neuropil signal. **c–e,** Cellular sensory properties pooled from two independent cohorts of Emx1-Cre×*Syngap1* cKO mice in response to 5 pulses at 5 Hz whisker stimulations under anesthesia. (**c**) Scatter plot showing fraction of responding cells in WT and Het mice (unpaired t test, $t_{14}=0.85$, $P=0.41$; $n=8$ WT mice, 8 Het mice). (**d,e**) Cumulative probability and scatter plots (insets) of (**d**) $\Delta F/F$ amplitudes (KS test, $P=0.016$; $n=327$ WT neurons, 306 Het neurons) and (**e**) response probabilities (KS test, $P=8.2\times10^{-5}$) in responding neurons. Data obtained from 1,671 neurons in 55 imaging planes from 8 WT mice and 1,877 neurons in 58 imaging planes from 8 Het mice. **f–h,** Cellular sensory properties pooled from two independent cohorts of Cux2-Cre^ERT2 ×*Syngap1* cKO mice in response to 5 pulses at 5 Hz whisker stimulations under anesthesia. (**f**) Scatter plot showing fraction of responding cells in WT and Het mice (unpaired t test; $t_{14}=0.56$, $P=0.58$; $n=8$ WT mice, 8 Het mice). (**g,h**) Cumulative probability and scatter plots (insets) of (**g**) $\Delta F/F$ amplitudes (KS test, $P=0.0002$; $n=435$ WT neurons, 445 Het neurons) and (**h**) response probabilities (KS test, $P=0.67$) in responding neurons. Data obtained from 2,015 neurons in 57 imaging planes from 8 WT mice and 1,901 neurons in 56 imaging planes from 8 Het mice. **i–k,** Cellular sensory properties pooled from two independent cohorts of Rpb4-Cre×*Syngap1* cKO mice in response to 5 pulses at 5 Hz whisker stimulations under anesthesia. (**i**) Scatter plot showing fraction of responding cells in WT and Het mice (unpaired t test; $t_{13}=0.64$, $P=0.53$; $n=8$ WT mice, $n=7$ Het mice). Cumulative probability and scatter plots (insets) of (**j**) $\Delta F/F$ amplitudes (KS test, $P=0.74$; $n=340$ WT neurons, 317 Het neurons) and (**k**) response probabilities (KS test, $P=0.26$) in responding neurons. Data obtained from 1,684 neurons in 56 imaging planes from 8 WT mice and 1,411 neurons in 46 imaging planes from 7 Het mice. In scatter plots, open circles are animal means, closed circles are individual cells, black lines indicate population means, and error bars indicate s.e.m. All statistical tests were two-sided.
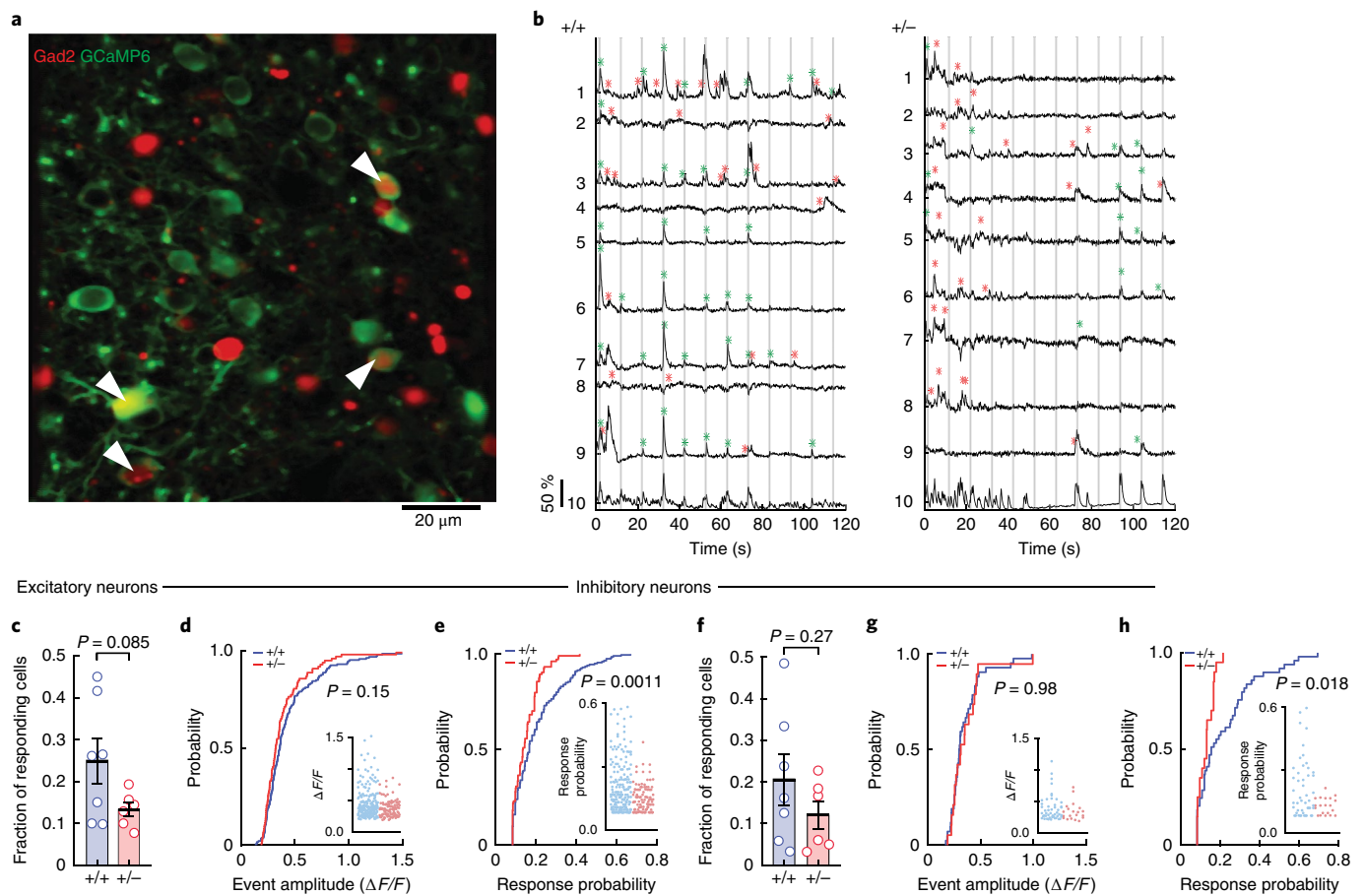
Fig. 5 | Reduced sensory responsiveness in both excitatory and inhibitory neuronal populations in L2/3 SSC of *Syngap1* mutants. a, Representative in vivo two-photon microscopy image of L2/3 SSC of a Gad2-T2A-NLS-mCherry × *Syngap1* WT mouse expressing GCaMP6s (green) and mCherry (red). White arrows indicate mCherry⁺ (inhibitory) neurons expressing GCaMP6s. **b**, Representative ΔF/F traces of 9 (1–9) excitatory neurons in WT and Het mice in response to 5 passive whisker deflections at 5 Hz. Gray vertical lines indicate the timing of whisker stimuli. Green asterisks indicate calcium events within the response detection window. Red asterisks show spontaneous calcium events. ROI 10 is the neuropil signal. **c–h**, Cellular sensory properties of excitatory (**c–e**) and inhibitory (**f–h**) neurons. (**c**) Scatter plot showing fraction of excitatory neurons responsive to whisker stimulation (unpaired t test; $t_{11} = 1.891$, $P = 0.0853$; $n = 7$ WT mice, 6 Het mice). (**d,e**) Cumulative probability and scatter plots (insets) of (**d**) ΔF/F amplitudes (KS test, $P = 0.1543$; $n = 200$ WT neurons, 104 Het neurons) and (**e**) response probabilities (KS test, $P = 0.0011$) in responding excitatory neurons. (**f**) Scatter plot showing fraction of inhibitory neurons responsive to whisker stimulation (unpaired t test; $t_{11} = 1.164$, $P = 0.2691$; $n = 7$ WT mice, 6 Het mice). (**g,h**) Cumulative probability and scatter plots (insets) of (**g**) ΔF/F amplitudes (KS test, $P = 0.9848$; $n = 49$ WT neurons, 20 Het neurons) and (**h**) response probabilities (KS test, $P = 0.0176$) in responding inhibitory neurons. Data in this figure were pooled from two independent cohorts of animals and thus obtained from 850 excitatory and 240 inhibitory cells in 48 imaging planes from 7 WT mice and 825 excitatory and 193 inhibitory cells in 45 imaging planes from 6 Het mice. Open circles are animal means, closed circles are individual cells, black lines indicate population means, and error bars indicate s.e.m. All statistical tests were two-sided.

population of excitatory neurons, *Syngap1* disruption appeared to preferentially affect the most active cells. Similarly, there was a reduction in whisker-evoked neuronal activation from mCherry⁺ (inhibitory) neurons (Fig. 5f–h). A reduced probability of firing in inhibitory neurons in response to whisker stimulation suggests that *Syngap1* heterozygosity did not result in an overactive population of GABA-releasing neurons.

Deficits in touch-related cortical circuit activation in *Syngap1* mice are associated with reduced synaptic and intrinsic excitability of upper-lamina SSC neurons. The above result prompted us to investigate impaired excitation as a possible cause of reduced sensory-related activity within upper-lamina SSC networks. We performed in vivo whole-cell patch-clamp recordings in L2/3 neurons of barrel cortex to determine how *Syngap1* heterozygosity affects whisker-evoked synaptic potentials in anesthetized mice. Synaptic depolarization in response to passive whisker stimulation was reduced in Het mice compared to WT mice (Fig. 6a–c), a find-

ing consistent with reduced whisker-driven cellular activity within upper-layer SSC circuits. We did not observe any alterations in spontaneous up–down state properties or changes in resting membrane potential in neurons from Het mice (Supplementary Table 3).

We further hypothesized that structural impairments in L2/3/4 neurons may contribute to reduced whisker-evoked feedforward excitation in upper-lamina SSC circuits. L4 stellate cells in SSC receive the bulk of sensory-related information arriving from subcortical areas[8,34]. Anatomical assessment of digitally reconstructed L4 neurons showed they were smaller in *Syngap1* Het mice than in WT mice (Fig. 7a), with reduced overall complexity and length in dendritic arbors. Dendrites from L4 neurons also had reduced spine density (Fig. 7b). Similar anatomical disruptions were found within dendrites and spines of L2/3 pyramidal cells from Het mice (Fig. 7c,d), which receive dense ascending projections from L4 stellate cells that relay sensory-related information to superficial neurons. These findings suggested that there were fewer excitatory synapses in upper-lamina SSC neurons.
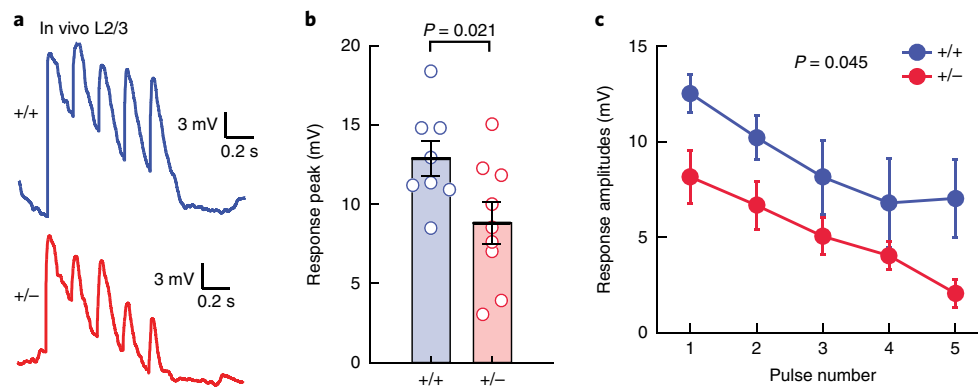
Fig. 6 | In vivo patch clamp reveals that L2/3 SSC neurons in *Syngap1* mutants have reduced sensory-evoked synaptic input. a, Representative in vivo traces for whole-cell patch-clamp experiments in response to passive whisker stimulations (5 pulses at 5 Hz). **b**, Scatter plot showing the overall response peaks (*t* test: $t_{15} = 2.59$, $P = 0.021$; $n = 8$ WT, 9 Het mice). Open circles represent animal means, black lines indicate population means, and error bars indicate s.e.m. **c**, Individual response amplitudes (two-way RM-ANOVA; genotype: $F_{1,14} = 4.82$, $P = 0.045$; genotype × stimulus: $F_{4,56} = 0.72$, $P = 0.58$) in response to whisker stimulation in L2/3 neurons from in vivo patch clamp recordings. Closed circles represent population means and error bars indicate s.e.m. Data obtained from two cohorts of *Syngap1* animals. All statistical tests were two-sided.
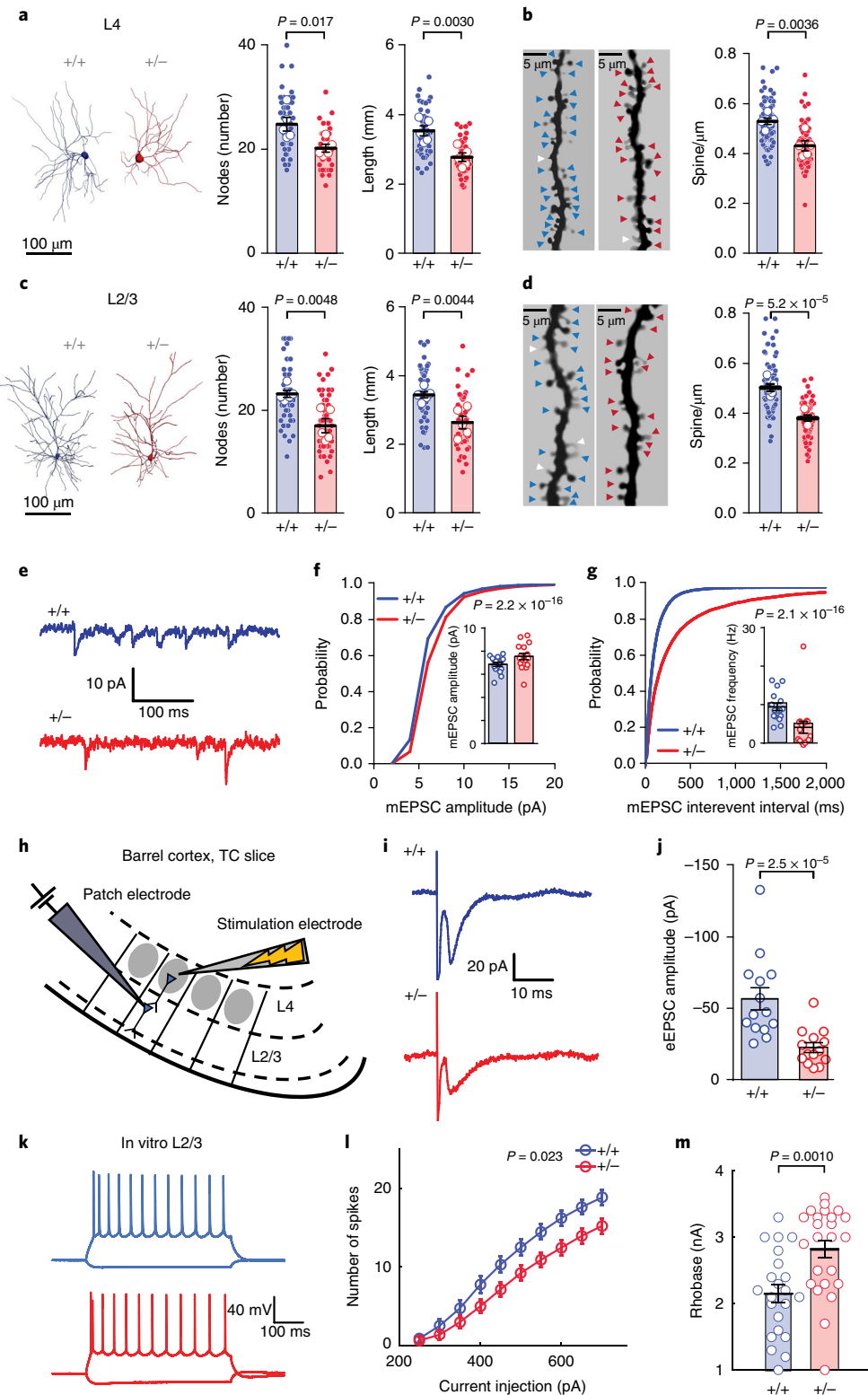
Patch-clamp recordings from L2/3 SSC neurons prepared from acute brain slices supported this idea. Miniature excitatory post-synaptic current (mEPSC) frequency was dramatically reduced in neurons from Het mice (Fig. 7e,g). Notably, mEPSC amplitude was slightly increased in these same neurons (Fig. 7f), possibly reflecting homeostatic compensation arising from too few excitatory synaptic inputs[35]. To directly measure feedforward excitation within upper-lamina SSC circuits, we recorded synaptic currents in SSC L2/3 neurons evoked by electrical stimulation of L4 (Fig. 7h). Evoked synaptic currents in L2/3 neurons were reduced in amplitude in Het mice compared to WT mice (Fig. 7i,j). Finally, it is known that homeostatic compensation of both synaptic and intrinsic neuronal properties contributes to producing stable firing rates. We therefore wondered how intrinsic excitability mechanisms might be engaged to potentially counteract changes in reduced synaptic input onto, and overall activity within, upper-lamina L2/3 SSC neurons. Unexpectedly, intrinsic excitability in L2/3 neurons was decreased in *Syngap1* Het mice compared to controls (Fig. 7k–m), which may also contribute to the reduced activity observed in these neurons.

Touch-related behaviors are impaired in *Syngap1* mice. Impairments in SSC circuit function in *Syngap1* mice may be predictive of whisker-dependent behavioral deficits. To test this, we first explored the ability of constitutive *Syngap1* mice to detect novel objects exclusively through touch. Notably, *Syngap1* mice are known to have normal novel object recognition memory[36]. Therefore, we could determine how potential deficits in touch perception may influence novelty detection of similar objects that differ only by subtle changes in their surface texture (Fig. 8a). Individual objects with differing textures were equally salient to test subjects (Fig. 8b). During the learning phase, WT mice and Het mice explored identical objects for a proportionally similar amounts of time, though Het mice spent more total time exploring objects overall (Fig. 8c,d), which may be related to increased locomotion in this line[37]. During testing with inclusion of the novel object, WT mice distinguished between distinct textures, as evidenced by increased exploration of the novel relative to familiar object (Fig. 8c,e). In contrast, Het mice failed to show a bias toward the novel object (Fig. 8d,e). Thus, Het mice did not discriminate between similar objects that differed only by surface texture.

Fig. 7 | *Syngap1* heterozygosity degrades synaptic connectivity and reduces intrinsic excitability of upper layer SSC neurons. a,c, Representative three-dimensional reconstruction of (**a**) L4 and (**c**) L2/3 SSC excitatory neurons depicting dendritic complexity (left) and scatter plot (right) showing the total length and numbers of nodes using Sholl analysis (L4: total length, $n = 5$ WT mice, 5 Het mice, unpaired *t* test, $t_8 = 4.002$, $P = 0.0030$; number of nodes, unpaired *t* test, $t_8 = 3.017$, $P = 0.0166$; L2/3: total length, $n = 5$ WT mice, 6 Het mice, unpaired *t* test, $t_9 = 3.7713$, $P = 0.0044$; number of nodes, unpaired *t* test, $t_9 = 3.7090$, $P = 0.0048$, from a single cohort of animals). **b,d**, Examples of (**b**) L4 and (**d**) L2/3 apical dendrites (left) and scatter plots (right) depicting the density of dendritic spines (L4 spine density: $n = 5$ WT mice, 5 Het mice, unpaired *t* test, $t_8 = 4.059$, $P = 0.0036$; L2/3 spine density: $n = 5$ mice, 5 Het mice, unpaired *t* test, $t_8 = 7.80$, $P = 5.2 \times 10^{-5}$, from a single cohort of animals). **e**, Representative traces depicting L2/3 excitatory neuron mEPSCs from acute WT and Het thalamocortical (TC) slices. **f,g**, Cumulative probability and scatter plots (insets) of (**f**) mEPSC amplitudes (KS test, $P = 2.2 \times 10^{-16}$) and (**g**) mEPSC interevent intervals (KS test, $P = 2.1 \times 10^{-16}$). Data were acquired from a single cohort of animals with $n = 7,986$ mEPSC events from 16 neurons in 4 WT mice and $n = 6,765$ mEPSC events from 16 neurons in 4 Het mice. **h**, Cartoon depicting experimental setup for investigating feedforward excitation in L2/3 excitatory neurons from L4. **i**, Representative traces depicting L2/3 excitatory neuron eEPSCs from acute WT and Het TC slices. **j**, Scatter plot of eEPSC amplitudes in L2/3 following stimulation of L4 (Mann–Whitney test, $U = 14.00$, $P = 2.5 \times 10^{-5}$; data obtained from a single cohort of animals; $n = 14$ neurons from 4 WT mice, $n = 14$ neurons from 4 Het mice). **k,l**, Representative (**k**) current-clamp traces from L2/3 excitatory neurons from acute WT and Het TC slices and (**l**) graph depicting a decrease in the number of spikes (two-way RM-ANOVA, genotype: $F_{1,46} = 5.51$, $P = 0.023$; genotype × stimulus: $F_{9,414} = 5.46$, 9.0×10^{-9}; $n = 22$ neurons from 5 WT mice, $n = 26$ neurons from 6 Het mice) in response to current injections. **m**, Scatter plot showing increased rheobase (Student's *t* test: $t_{44} = 3.50$, $P = 0.0010$) in the same set of neurons as in **l**. Data were obtained from a single cohort of animals. For morphology data, open circles are animal means, closed circles are individual cells, black lines indicate population means, error bars indicate s.e.m., colored triangles represent spines (blue, WT; red, Het), and white triangles represent filopodia. For **f**, **g**, **j**, and **m**, open circles are individual cells, black lines indicate population means, and error bars indicate s.e.m. For **l**, circles represent population means and error bars indicate s.e.m. All statistical tests were two-sided.

We next used a discrimination task that requires the perception of a stimulus similar to those used for evoking neuronal activity in our functional studies (Figs. 1–6). We selected a go or no-go (go/no-go) framework, in which water-deprived mice learn to perceptually report passive deflections of their whiskers by licking a water-dispensing port during a short 'answer' period[38,39] (Fig. 8f). This type of learning experiment is attractive for probing touch-related behaviors because it requires an intact ability to perceive a whisker

stimulation[39] and activation of whisker-responsive cortical circuits to sufficiently drive learning[40]. Task performance is quantified by the probability of correct choices during two trial types, 'go' (presence of whisker stimulus cue) and 'no-go' (absence of whisker cue; Fig. 8g). WT mice learned to discriminate between trial types after sufficient training (Fig. 8h and Supplementary Fig. 4a,b), with trial discrimination dependent on the strength of whisker stimulation (Fig. 8i,j), confirming that task performance was driven by a stimu-

lus precept computed by the function of whisker-sensitive circuits. Age-matched cohorts of *Syngap1* WT mice and Het mice were then trained, with 86% of WT mice and 0% of Het mice reaching the training goals (Fig. 8k). WT mice learned to lick during go trials and withhold licks during no-go trials (Fig. 8h and Supplementary Fig. 4a,b). In contrast, Het mice did not improve accuracy in either trial type, likely explaining their static task performance over time (Fig. 8l and Supplementary Fig. 4c,d). Notably, we observed a significant difference between genotypes in the fraction of correct answers over the entire training interval (Fig. 8m) and in the trial discrimination index (Fig. 8n), an objective measure of overall task performance at the completion of training. There was no difference between genotypes in relative weight gain or loss over the training interval (Supplementary Fig. 4e), and Het mice exhibited normal licking, indicating familiarity with use of the port (Supplementary Fig. 4f,g). There was also no difference between genotypes in the response times for either trial type (Supplementary Fig. 4h,i) or total trials during training (Supplementary Fig. 4j–l). We also found no evidence of impulsive responding in Het mice (Supplementary Fig. 4m–o). Together, these data indicate that poor task performance in Het mice was not related to an obvious lack of motivation, training participation, or generalized impairment in the instrumental response.

Discussion

The principal finding of this study is that disease-linked *SYNGAP1/Syngap1* variants led to impaired sensory processing. Sensory abnormalities are common in NDD populations[41,42]. Moreover, there is a correlation between the severity of sensory disruptions and behavioral phenotypes in ASD populations[43]. Human imaging studies from NDD[5] and schizophrenia patients[6] have identified altered functioning of primary sensory areas, leading to the idea that altered sensory processing contributes directly to the complex phenotypes observed in patients. However, the neurophysiological mechanisms that lead to NDD-associated sensory impairments are

poorly understood. By mining a *SYNGAP1* patient registry within a retrospective natural history study, we confirmed that clinically significant sensory alterations exist in patients with *SYNGAP1* haploinsufficiency, including abnormal responses to painful tactile stimuli and unusual touch-related behaviors (Supplementary Table 2). Moreover, using *Syngap1* mouse models, we uncovered unexpected circuit-level mechanisms consistent with impaired touch-related cortical sensory processing. Thus, reverse translation of NDDs caused by single rare variants, such as *SYNGAP1*, hold promise for better understanding these pathobiological mechanisms.

Our findings demonstrate that *Syngap1* heterozygosity reduces activity within upper-lamina SSC circuits in awake *Syngap1* mice. Reduced measures of sensory-evoked activity in vivo persisted in awake animals with paralyzed whiskers and in animals under anesthesia. These results were unexpected because many prior reports describe increased excitability and synaptic function in neurons from *Syngap1*-heterozygous mutant animals[23,24,27,44–47]. Indeed, *Syngap1* heterozygosity is believed to generally enhance neuronal excitation through shifting the synaptic excitation–inhibition ratio in several types of neurons in areas of the brain linked directly to cognitive processing[23,44,48,49]. *Syngap1* is a risk factor for severe epilepsy[21], and prior studies in the *Syngap1* mouse line used in this study have described seizure and circuit hyperexcitability in the hippocampus and prefrontal cortex[23,24]. *Syngap1* pathogenicity also accelerates the maturation of excitatory synapses during development, including several inputs within the hippocampus[23] and the thalamocortical synapse in L4 SSC[27]. Moreover, *Syngap1* pathogenicity reduces the level of GABAergic connectivity onto SSC pyramidal neurons[26]. This loss of inhibitory control contributes to changes in oscillatory cortical rhythms in *Syngap1* mice and is also consistent with increased excitability of neural circuits. The most parsimonious explanation for the differences between these prior reports and the current study is that *Syngap1* heterozygosity has cell- and region-specific effects. For instance, L2/3/4 SSC neurons in adult constitutive *Syngap1* mice had smaller dendritic fields with

Fig. 8 | Impaired texture discrimination and whisker-dependent go/no-go task performance in *Syngap1* mice. a, Cartoons depicting different texture roughness of the objects used in novel texture discrimination task and relative protocol. **b**, Scatter plot showing no preference in exploring textures T1 or T2 (T1 vs. T2: $n = 12$ mice; unpaired t test, $t_{22} = 0.0016$, $P = 0.9986$). **c,d**, Box plots (solid line represents median, box represents interquartile range, and whiskers represent maximum and minimum values) depicting time spent exploring identically textured objects during the learning phase and time spent exploring the novel (T2) and the old (T1) object for (**c**) WT and (**d**) Het groups (WT mice, Friedman test: $n = 18$ mice, $\chi^2(3) = 28.87$, exact sign, $P = 1.4206 \times 10^{-7}$; HET mice, Friedman test: $n = 15$ mice, $\chi^2(3) = 15.24$, exact sign, $P = 0.0016$; pairwise comparisons: WT learning vs. testing, sign test, $n = 18$ mice, $Z = 4.007$ $P = 0.00006$; Het learning vs. testing, sign test, $n = 15$ mice, $Z = 2.065$, $P = 0.04$, nonsignificant (n.s.); WT learning vs. Het learning, Mann–Whitney U test: $Z = -2.567$ $P = 0.01$; WT testing vs. Het testing, Mann–Whitney U test: $Z = -2.821$ $P = 0.0048$). Statistical significance was accepted at the $P < 0.03125$. **e**, Scatter plot showing exploration index for animals in **c** and **d** (WT mice, paired t test: $t_{17} = 4.707$, $P = 0.0002$; Het mice, paired t test: $t_{14} = 1.641$, $P = 0.123$; one-sample test: WT learning, $t_{17} = 1.555$, $P = 0.138$; WT testing, $t_{17} = 8.579$, $P = 1.39 \times 10^{-7}$; Het learning, $t_{14} = -2.164$, $P = 0.048$, n.s.; Het testing, $t_{14} = -2.415$, $P = 0.03$, n.s.). **f**, Cartoon representation of go/no-go setup. Water-restricted, headfixed mice were rewarded with water for licking a lick-port in response to a passive whisker (C2) deflection. **g**, Detection task trial structure for Step 2 training. Go trials are identical to no-go trials, except for the passive whisker deflection. Note that no-go trials included activation of a 'dummy' piezo not attached to any whisker to control for noise and vibration associated with piezo activation. **h**, Step 2 training learning curve for WT mice showing the probability of licking (P(lick)) on go (black, hit) or no-go (blue, false alarm) trials ($n = 7$ mice; two-way RM-ANOVA with Bonferroni's multiple comparison, trial type: $F_{1,6} = 67.19$, $P = 0.0002$; session: $F_{15,90} = 0.4827$, $P = 0.9437$; trial type × session: $F_{15,90} = 5.86$, $P = 2.9 \times 10^{-8}$). **i,j**, Reductions in angular velocity of whisker deflections (**i**) impairs the ability of good-performing WT mice to discriminate between trial types ($n = 6$ mice; two-way RM-ANOVA with Bonferroni's multiple comparison, trial type: $F_{1,5} = 471.1$, $P = 3.9 \times 10^{-6}$; velocity: $F_{3,15} = 1.469$, $P = 0.263$; trial type × velocity: $F_{3,15} = 30.12$, $P = 1.4 \times 10^{-6}$) and (**j**) results in a reduced discrimination index ($n = 6$ mice; RM-ANOVA with Bonferroni's multiple comparison, $F_{3,15} = 24.52$, $P = 4.9 \times 10^{-6}$). **k**, Proportion of mice to learn (performers (P) vs. nonperformers (NonP)) the task ($n = 7$ WT mice, 7 Het mice: Fisher's exact test: $P = 0.0047$). **l**, Step 2 training learning curve for Het mice ($n = 7$ mice; two-way RM-ANOVA with Bonferroni's multiple comparison, trial type: $F_{1,6} = 8.44$, $P = 0.027$; session: $F_{15,90} = 2.416$, $P = 0.0054$; trial type × session: $F_{15,90} = 0.8852$, $P = 0.5825$). **m**, Learning curves depicting the fraction of total trials correct in Step 2 training (WT $n = 7$, Het $n = 7$; two-way RM-ANOVA with Bonferroni's multiple comparison, Genotype: $F_{1,12} = 10.13$ $P = 0.0079$; Session: $F_{15,180} = 3.665$ $P = 1.4 \times 10^{-5}$; Genotype*Session interaction: $F_{15,180} = 4.398$ $P = 5.2 \times 10^{-7}$). Solid black line indicates performance criteria for total trials correct. **n**, Scatter plot showing the discrimination index at the completion of Step 2 training ($n = 7$ WT, 7 Het mice; unpaired t test, $t_{12} = 4.281$, $P = 0.0011$). Data for both novel texture discrimination and go/no-go tasks were obtained from two independent cohorts of animals. Open circles are individual animals, closed circles and solid black horizontal lines indicate population means, and error bars or shaded area represent s.e.m., except for boxplots in **c** and **d**, which are described above. *$P < 0.05$, **$P < 0.01$, ***$P < 0.001$, ****$P < 0.0001$ for post hoc multiple comparisons. Solid black and blue dashed lines in **h**, **i**, and **l** indicate performance criteria for hit and false alarm, respectively. All statistical tests were two-sided.
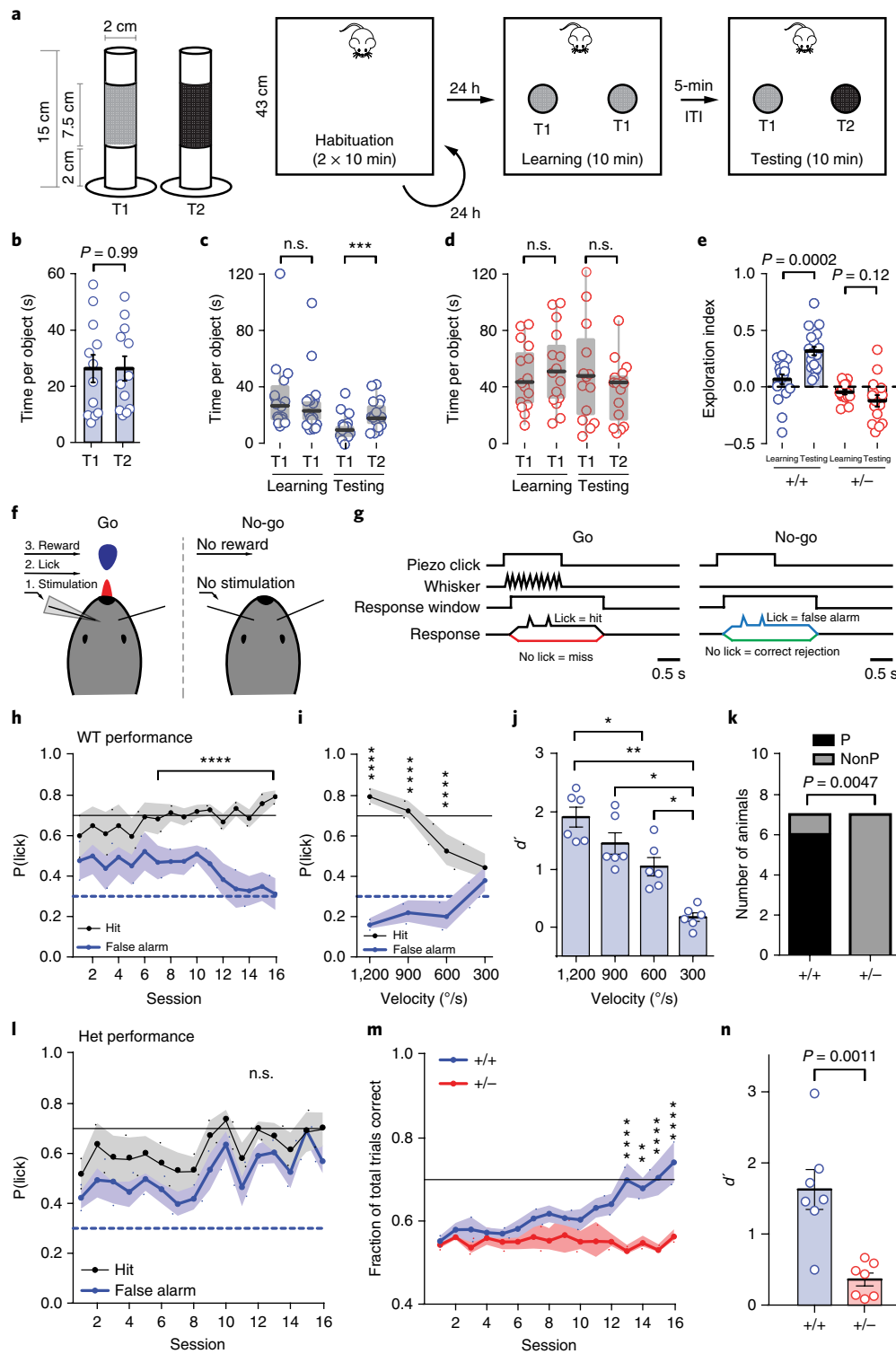
reduced spine density, which contributed to reduced feedforward excitation during sensory stimulation. However, deep-layer SSC neurons from adult *Syngap1* mutants were previously shown to have normal arbor sizes and spine densities[50]. Therefore, the overall impact of *Syngap1* heterozygosity on brain function is defined by a range of circuit-specific impairments that disrupt neuronal excitability and function in complex ways. Our findings, therefore, give insight into the complexity of how a single gene causally linked to severe ID and epilepsy can disrupt the structure and function of neurons and circuits linked to cognitive processes. We propose a generalizable scheme in which interactions among region-specific circuit pathologies caused by causally linked NDD risk variants drive complex cognitive and behavioral phenotypes observed in affected individuals. The challenge will be to understand how disparate circuit pathologies interact to disrupt behavior, impair cognition, and promote seizures. Furthermore, it will be important to understand to what extent other highly penetrant ID risk genes cause similarly complex region- and/or circuit-specific pathologies.

Our results support the conclusion that measures of reduced neuronal activity within upper-lamina SSC circuits in *Syngap1* mice were caused by a combination of lower intrinsic excitability and reduced synaptic connectivity onto L2/3 neurons in this area. This interpretation is supported by several key pieces of data. First, measures of reduced activity of SSC L2/3 neurons can be attributed to effects of *Syngap1* within this cellular population. Restricting *Syngap1* heterozygosity to forebrain glutamatergic neurons and some glia (that is, EMX1⁺ populations) was sufficient to impair SSC neuronal activity evoked by passive whisker deflections. This indicates that a primary cause of impaired sensory-evoked activity within *Syngap1* mutants arises, at least in part, from altered function of cortical circuits, rather than from disruptions in sensory coding occurring in subcortical areas, such as in the mechanoreceptor neurons or thalamic relays. Second, evoked L2/3 SSC neuronal activation was depressed in both GABAergic and glutamatergic cellular populations, indicating that reduced activity was not a consequence of increased inhibition. Third, in vivo patch-clamp recording demonstrated reduced whisker-evoked membrane depolarization in L2/3 neurons from Het mice, which is consistent with our primary observation of reduced cellular activity of neurons in this area. In measurements from acute slices, these neurons also had reduced intrinsic excitability, which may contribute to reduced membrane depolarization observed in vivo. Fourth, we observed that both L4 and L2/3 neurons from Het mice had smaller dendritic fields. We also observed that these shortened dendritic fields contained fewer dendritic spines. This anatomical defect translated into reduced functional synaptic connectivity, as we observed reduced mEPSC frequency in Het neurons even though there was a slight increase in mEPSC amplitude. Increased mEPSC amplitudes in L2/3 neurons from Het mice is consistent with our prior observation of larger dendritic spines in these cells[50], which may be a homeostatic adaptation to neurons that have reduced activity[35]. We also observed direct evidence of reduced feedforward excitation within the upper lamina of SSC. There was a substantial decrease in synaptic input from L4 to 2/3 in thalamocortical slices prepared form *Syngap1* mice. In this study we were able to show that large impairments in synaptic function within whisker-responsive circuits translated into a substantial reduction in touch-related proxy measures of somatic spiking (that is, superthreshold somatic GCAMP6 events) within these same circuits. Taken together, these data are consistent with a model in which L2/3 neurons in *Syngap1* mice poorly encode incoming sensory information due to reduced synaptic excitation within the upper lamina of SSC. Given that L2/3 neurons integrate bottom-up sensory codes with top-down modulatory information[7], it is possible that the cortex-specific circuit pathologies uncovered in this study disrupt sensory processing related to learning and/or behavioral adaptations. Future studies will be necessary to causally link activity deficits within cortical circuits that respond to sensory input in *Syngap1* mice to relevant behavioral phenotypes such as poor learning.

Online content

Any methods, additional references, Nature Research reporting summaries, source data, statements of data availability and associated accession codes are available at https://doi.org/10.1038/s41593-018-0268-0.

References

1. Sahin, M. & Sur, M. Genes, circuits, and precision therapies for autism and related neurodevelopmental disorders. *Science* **350**, aab3897 (2015).
2. Hull, J. V. et al. Resting-state functional connectivity in autism spectrum disorders: a review. *Front. Psychiatry* **7**, 205 (2017).
3. Just, M. A., Cherkassky, V. L., Keller, T. A. & Minshew, N. J. Cortical activation and synchronization during sentence comprehension in high-functioning autism: evidence of underconnectivity. *Brain* **127**, 1811–1821 (2004).
4. Zoghbi, H. Y. & Bear, M. F. Synaptic dysfunction in neurodevelopmental disorders associated with autism and intellectual disabilities. *Cold Spring Harb. Perspect. Biol.* **4**, a009886 (2012).
5. Robertson, C. E. & Baron-Cohen, S. Sensory perception in autism. *Nat. Rev. Neurosci.* **18**, 671–684 (2017).
6. Javitt, D. C. & Sweet, R. A. Auditory dysfunction in schizophrenia: integrating clinical and basic features. *Nat. Rev. Neurosci.* **16**, 535–550 (2015).
7. Peron, S. P., Freeman, J., Iyer, V., Guo, C. & Svoboda, K. A cellular resolution map of barrel cortex activity during tactile behavior. *Neuron* **86**, 783–799 (2015).
8. Feldmeyer, D. et al. Barrel cortex function. *Prog. Neurobiol.* **103**, 3–27 (2013).
9. Pluta, S. R., Lyall, E. H., Telian, G. I., Ryapolova-Webb, E. & Adesnik, H. Surround integration organizes a spatial map during active sensation. *Neuron* **94**, 1220–1233.e5 (2017).
10. Ogden, K. K., Ozkan, E. D. & Rumbaugh, G. Prioritizing the development of mouse models for childhood brain disorders. *Neuropharmacology* **100**, 2–16 (2016).
11. Hoischen, A., Krumm, N. & Eichler, E. E. Prioritization of neurodevelopmental disease genes by discovery of new mutations. *Nat. Neurosci.* **17**, 764–772 (2014).
12. Deciphering Developmental Disorders, S.; Deciphering Developmental Disorders Study. Large-scale discovery of novel genetic causes of developmental disorders. *Nature* **519**, 223–228 (2015).
13. Hamdan, F. F. et al. Mutations in *SYNGAP1* in autosomal nonsyndromic mental retardation. *N. Engl. J. Med.* **360**, 599–605 (2009).
14. Rauch, A. et al. Range of genetic mutations associated with severe non-syndromic sporadic intellectual disability: an exome sequencing study. *Lancet* **380**, 1674–1682 (2012).
15. Deciphering Developmental Disorders, S.; Deciphering Developmental Disorders Study. Prevalence and architecture of de novo mutations in developmental disorders. *Nature* **542**, 433–438 (2017).
16. O'Roak, B. J. et al. Recurrent de novo mutations implicate novel genes underlying simplex autism risk. *Nat. Commun.* **5**, 5595 (2014).
17. Hamdan, F. F. et al. De novo *SYNGAP1* mutations in nonsyndromic intellectual disability and autism. *Biol. Psychiatry* **69**, 898–901 (2011).
18. Berryer, M. H. et al. Mutations in *SYNGAP1* cause intellectual disability, autism, and a specific form of epilepsy by inducing haploinsufficiency. *Hum. Mutat.* **34**, 385–394 (2013).
19. Parker, M. J. et al. De novo, heterozygous, loss-of-function mutations in *SYNGAP1* cause a syndromic form of intellectual disability. *Am. J. Med. Genet. A.* **167A**, 2231–2237 (2015).
20. Mignot, C. et al. Genetic and neurodevelopmental spectrum of *SYNGAP1*-associated intellectual disability and epilepsy. *J. Med. Genet.* **53**, 511–522 (2016).
21. Carvill, G. L. et al. Targeted resequencing in epileptic encephalopathies identifies de novo mutations in *CHD2* and *SYNGAP1. Nat. Genet.* **45**, 825–830 (2013).
22. von Stülpnagel, C. et al. *SYNGAP1* mutation in focal and generalized epilepsy: a literature overview and a case report with special aspects of the EEG. *Neuropediatrics* **46**, 287–291 (2015).
23. Clement, J. P. et al. Pathogenic *SYNGAP1* mutations impair cognitive development by disrupting maturation of dendritic spine synapses. *Cell* **151**, 709–723 (2012).
24. Ozkan, E. D. et al. Reduced cognition in *Syngap1* mutants is caused by isolated damage within developing forebrain excitatory neurons. *Neuron* **82**, 1317–1333 (2014).
25. Agency for Healthcare Research and Quality. *Registries for Evaluating Patient Outcomes: A User's Guide [Internet]: Rare Disease Registries.* (Gliklich, R. E., Dreyer, N. A., & Leavy, M. B.) Chapter 20 (US Department of Health & Human Services, Rockville, MD, USA, 2014).
26. Berryer, M. H. et al. Decrease of SYNGAP1 in GABAergic cells impairs inhibitory synapse connectivity, synaptic inhibition and cognitive function. *Nat. Commun.* **7**, 13340 (2016).
27. Clement, J. P., Ozkan, E. D., Aceti, M., Miller, C. A. & Rumbaugh, G. SYNGAP1 links the maturation rate of excitatory synapses to the duration of critical-period synaptic plasticity. *J. Neurosci.* **33**, 10447–10452 (2013).
28. Dana, H. et al. Thy1-GCaMP6 transgenic mice for neuronal population imaging in vivo. *PLoS One* **9**, e108697 (2014).
29. Gonçalves, J. T., Anstey, J. E., Golshani, P. & Portera-Cailliau, C. Circuit level defects in the developing neocortex of Fragile X mice. *Nat. Neurosci.* **16**, 903–909 (2013).
30. Wolfe, J., Houweling, A. R. & Brecht, M. Sparse and powerful cortical spikes. *Curr. Opin. Neurobiol.* **20**, 306–312 (2010).
31. Margolis, D. J. et al. Reorganization of cortical population activity imaged throughout long-term sensory deprivation. *Nat. Neurosci.* **15**, 1539–1546 (2012).

32. Gorski, J. A. et al. Cortical excitatory neurons and glia, but not GABAergic neurons, are produced in the Emx1-expressing lineage. *J. Neurosci.* **22**, 6309–6314 (2002).

33. Gray, L. T. et al. Layer-specific chromatin accessibility landscapes reveal regulatory networks in adult mouse visual cortex. *eLife* **6**, e21883 (2017).

34. Diamond, M. E. & Arabzadeh, E. Whisker sensory system - from receptor to decision. *Prog. Neurobiol.* **103**, 28–40 (2013).

35. Nelson, S. B. & Valakh, V. Excitatory/inhibitory balance and circuit homeostasis in autism spectrum disorders. *Neuron* **87**, 684–698 (2015).

36. Muhia, M., Yee, B. K., Feldon, J., Markopoulos, F. & Knuesel, I. Disruption of hippocampus-regulated behavioural and cognitive processes by heterozygous constitutive deletion of SynGAP. *Eur. J. Neurosci.* **31**, 529–543 (2010).

37. Guo, X. et al. Reduced expression of the NMDA receptor-interacting protein SynGAP causes behavioral abnormalities that model symptoms of schizophrenia. *Neuropsychopharmacology* **34**, 1659–1672 (2009).

38. Sachidhanandam, S., Sermet, B. S. & Petersen, C. C. H. Parvalbumin-expressing GABAergic neurons in mouse barrel cortex contribute to gating a goal-directed sensorimotor transformation. *Cell Rep.* **15**, 700–706 (2016).

39. Yang, H., Kwon, S. E., Severson, K. S. & O'Connor, D. H. Origins of choice-related activity in mouse somatosensory cortex. *Nat. Neurosci.* **19**, 127–134 (2016).

40. Sachidhanandam, S., Sreenivasan, V., Kyriakatos, A., Kremer, Y. & Petersen, C. C. Membrane potential correlates of sensory perception in mouse barrel cortex. *Nat. Neurosci.* **16**, 1671–1677 (2013).

41. Ben-Sasson, A. et al. A meta-analysis of sensory modulation symptoms in individuals with autism spectrum disorders. *J. Autism Dev. Disord.* **39**, 1–11 (2009).

42. Marco, E. J., Hinkley, L. B., Hill, S. S. & Nagarajan, S. S. Sensory processing in autism: a review of neurophysiologic findings. *Pediatr. Res.* **69**, 48R–54R (2011).

43. Robertson, A. E. & Simmons, D. R. The relationship between sensory sensitivity and autistic traits in the general population. *J. Autism Dev. Disord.* **43**, 775–784 (2013).

44. Araki, Y., Zeng, M., Zhang, M. & Huganir, R. L. Rapid dispersion of SynGAP from synaptic spines triggers AMPA receptor insertion and spine enlargement during LTP. *Neuron* **85**, 173–189 (2015).

45. Kopanitsa, M. V. et al. Chronic treatment with a MEK inhibitor reverses enhanced excitatory field potentials in *Syngap1*^{+/−} mice. *Pharmacol. Rep.* **70**, 777–783 (2018).

46. Rumbaugh, G., Adams, J. P., Kim, J. H. & Huganir, R. L. SynGAP regulates synaptic strength and mitogen-activated protein kinases in cultured neurons. *Proc. Natl. Acad. Sci. USA* **103**, 4344–4351 (2006).

47. Vazquez, L. E., Chen, H. J., Sokolova, I., Knuesel, I. & Kennedy, M. B. SynGAP regulates spine formation. *J. Neurosci.* **24**, 8862–8872 (2004).

48. Walkup, W. G. et al. A model for regulation by SynGAP-alpha1 of binding of synaptic proteins to PDZ-domain 'Slots' in the postsynaptic density. *eLife* **5**, e16813 (2016).

49. Zeng, M., Bai, G. & Zhang, M. Anchoring high concentrations of SynGAP at postsynaptic densities via liquid-liquid phase separation. *Small GTPases* https://doi.org/10.1080/21541248.2017.1320350 (2017).

50. Aceti, M. et al. *Syngap1* haploinsufficiency damages a postnatal critical period of pyramidal cell structural maturation linked to cortical circuit assembly. *Biol. Psychiatry* **77**, 805–815 (2015).

Acknowledgements

Author contributions

S.D.M. performed experiments, designed experiments, analyzed data, co-wrote the manuscript, and edited the manuscript. E.D.O. performed experiments, designed experiments, analyzed data, and edited the manuscript. M.A. performed experiments, designed experiments and analyzed data. S.M. performed experiments, designed experiments, and analyzed data. E.M. performed experiments, designed experiments, and analyzed data. M.W. performed experiments, designed experiments, and analyzed data. N.L. performed experiments and analyzed data. T.V. performed experiments and analyzed data. M.A.G. designed experiments and interpreted data. J.M.C. designed experiments and interpreted data. J.L.H. performed experiments, designed experiments, analyzed data, interpreted data, and edited the manuscript. C.A.M. designed experiments, interpreted data, and edited the manuscript. G.R. conceived the study, designed experiments, interpreted data, co-wrote the manuscript, and edited the manuscript.

Competing interests

The authors declare no competing financial interests. M.W. is a paid employee of Bridge-the-GAP Educational Research Foundation. G.R. and J.L.H. are unpaid scientific advisors to Bridge-the-GAP Educational Research Foundation.

Additional information

Supplementary information is available for this paper at https://doi.org/10.1038/s41593-018-0268-0.

Reprints and permissions information is available at www.nature.com/reprints.

Correspondence and requests for materials should be addressed to G.R.

Publisher's note: Springer Nature remains neutral with regard to jurisdictional claims in published maps and institutional affiliations.

Methods

Collection and analysis of data from the Retrospective SYNGAP1 Natural History Study Registry. The *SYNGAP1* Patient Registry (https://syngap1registry.iamrare.org) is funded through the National Organization of Rare Disorders. This study was approved through the Hummingbird Institutional Review Board and meets all relevant ethical regulations for protections for human subjects. It is actively managed by a board of trustees comprised of a team of seven stakeholders, including parents with affected children, clinician-scientists that care for MRD5 patients, and neurobiologists that study the gene. The *SYNGAP1* (MRD5) Natural History Study Registry is a retrospective longitudinal web-based observational natural history study. Parents or guardians provided informed consent before depositing medical history data into the registry. Participants with *SYNGAP1* (MRD5) will be followed throughout the course of their lives with either the participant or authorized respondents contributing data at varying intervals throughout the course of the study. Initially, when a new patient is registered, data is collected on demographics, quality of life, and medical history, including genetic reports, disease phenotypes, event episodic data, retrospective data, participant review of systems, and medication and diagnostic data. Each registrant is given a unique identifier to facilitate anonymization of patient data. Initial data collection is done through a series of questionnaires, including a survey of sensory and sensory-related issues. The structure of the database and all questionnaires were reviewed and approved by the members of the Board of Trustees.

To acquire information of possible sensory alterations in the *SYNGAP1* patient population, the registry database was queried for all entries that answered the sensory questionnaire. The questionnaires for each anonymized entry were then exported to a spreadsheet for analysis (Supplementary Table 1). Entries that noted obvious impairments in tactile alterations, typically though narrative descriptions in columns E, F, and/or K of Supplementary Table 1, were placed in Supplementary Table 2. The Registry was then revisited to determine whether genetic reports were available for these entries. Genetic reports were available for 17 of these 20 entries. The presence/absence of an anonymized genetic report for each entry was noted in Column A and for entries with a report, the type of variant was listed in Column B and pathogenicity in Column C. Notably, decisions on which entries to include in Supplementary Table 2 were made with no prior knowledge of each patient's genotype. Entries containing narratives were unedited, including spelling errors, except when necessary to protect patient information (that is, names were redacted).

Mice. All animal procedures were conducted in accordance with the National Institutes of Health *Guide for the Care and Use of Laboratory Animals*, and all protocols were approved by the Scripps Institutional Animal Care and Use Committee. The design and maintenance of the conventional and conditional *Syngap1* lines have been described previously[23,51]. Thy1-GCaMP6s4.3 (#024275), Gad2-NLS-mCherry (#023140), and TdTomato Ai9 (#007905) reporter lines were purchased from Jackson Laboratories. Rbp4-Cre (037128-UCD) and Cux2-CreERT2 (032779-MU) were purchased from MMRC. Both males and females were used in all experiments indiscriminately, except for the go/no-go task, in which only males were used. All animals were older than 6 weeks of age at the beginning of experiments. Data collection occurred from mice > 8 weeks of age. Mice were housed 4 or 5 per cage on a 12-h normal light–dark cycle, except for go/no-go experiments, for which mice were housed on a reverse light–dark cycle. For experiments requiring chronic cranial window and headpost implantation, mice were singly housed following surgery, with added environmental enrichment consisting of cardboard huts or plastic running wheels (Bio-Serv, Flemington, NJ) for the remainder of the study. Animals expressing the *Cux2-Cre^ERT2* allele were injected with tamoxifen (once) at P2 as previously described[50]. Data collection was semirandomized. Experimenters were blind to genotype at the time of data acquisition and analysis. Generation of multiple transgenic mouse lines was labor-, time-, and resource-intensive. Additionally, most experiments required 1–3 months to complete, even with small sample sizes. This prevented us from picking WT and Het animals completely at random. Therefore, to obtain comparable sample sizes between genotypes, animal cohorts were generated by allocating equal (if possible) numbers of age-matched *Syngap1* WT and Het littermates from separate litters, usually more than two. Then, animals were assigned a number to hide their genotype and/or group assignment. For imaging and behavior tasks, animals were recorded once per day in a randomized order while blinded to genotype. This process enabled balanced populations across experimental groups while minimizing potential biases. Only animals (or equivalent biological specimens) that died (or became nonresponsive) during the course of the study or data collection procedures were excluded from analysis. The Nature Research Reporting Summary contains additional details on data exclusions for specific experiments.

Intrinsic optical signal (IOS) imaging. Animals were anesthetized with 1.6 g/kg urethane (Sigma-Aldrich, St. Louis, MO), followed by implantation of a custom headplate. The skull was thinned by scraping gently with a scalpel, removing most of the spongy bone, but otherwise left intact. Following gluing of the headplate, the skull was sealed with 1.5% low-melting-point agarose dissolved in lactate ringer's solution under a glass coverslip. Imaging was performed under a 4× objective

on an upright microscope frame (BW51X; Olympus, Tokyo, Japan). The skull was illuminated with a 630-nm LED light mounted on the 4× objective[52]. The images were acquired with a Zeiss Axiocam camera (Carl Zeiss Microscopy Inc., Thornwood, NY) controlled by μManager software (Open Imaging, Inc.). Acquisition rate was approximately 10 Hz. Whiskers were deflected using a piezoelectric bending actuator controlled by a linear voltage amplifier (Piezo Systems Inc., Woburn, MA). A single sinusoidal wave with a 5-ms rise and a 5-ms decay time was generated using Clampex software (Molecular Devices, Sunnyville, CA). Bending of the piezo was calibrated using a laser based displacement device (LD1610-0.5 Micro-Epsilon, Raleigh, NC). A single whisker deflection was approximately 200 μm at 2 mm away from the whisker pad (~6° or 1,200 °/s). Each IOS imaging trial consisted of a 2-s baseline imaging period followed by 20 deflections at 10 Hz. We performed 50–70 trials for each whisker (now called an imaging session) and averaged them using IO and VSD Signal Processor plugin in ImageJ[52]. Images taken between 1 s and 3 s after the start of the stimulus were averaged and defined as the response. IOS images were obtained by calculating the (*response − baseline*)/*baseline* value for each pixel using custom scripts written in Matlab (MathWorks, Natick, MA), according to established procedures[53,54]. The animals that died during an intrinsic imaging experiment (due to anesthesia) or animals on which no visually reliable IOS map could be obtained (due to blood vessel contamination etc.) were excluded from the analysis (less than 5% of mice). Image analysis was performed by an investigator blind to animal genotype. Briefly, images were first filtered with a Gaussian filter. Afterwards a baseline and a response region were manually selected in the final IOS image to minimize contamination by blood vessels[53,55]. Response size was determined as the minimum value of the response region subtracted from the median of the baseline region. Image thresholding was performed in the response region to determine the area of activation. Thresholds based on the absolute response size are specified in the figures. Relative thresholding values were set at 50–80% of the response size for each image.

GCaMP widefield imaging (GWI). Thy1-GCaMP6s4.3 mice were implanted with a chronic cranial window according to established procedures[56,57]. Briefly, animals were anesthetized with Avertin (Tribromoethanol, Sigma-Aldrich, St. Louis, MO) and intraperitoneally injected with dexamethasone (4 mg/kg), Rimadyl (carprofen 10 mg/kg), and Enroflox (enrofloxacin 5 mg/kg). A 3-mm cranial window was made over the barrel cortex (A/P −2.0 mm, D/V +3.5 mm). The cranial window was sealed using two 3-mm glass coverslips glued onto a 5-mm glass coverslip. Animals were supplied with Rimadyl for 1 week in drinking water for pain management. Following 2–3 weeks recovery from the surgery, animals were anesthetized with 1.6 g/kg urethane. Widefield fluorescent imaging of GCaMP6 was performed through the cranial window using 490-nm illumination under a standard 4× objective. Signals were acquired using a standard eGFP epifluorescence filter set. Whisker deflection and acquisition parameters were the same as with the IOS imaging, although we varied the frequency and number of deflections as specified in the figures. Δ*F*/*F* images were obtained by calculating (*response − baseline*)/*baseline* for each pixel, similarly to intrinsic imaging. A fixed rectangle of 150 μm^2 centered at the functionally defined barrel center (90% relative thresholding) was used for creating individual and averaged Δ*F*/*F* traces. Bias was minimized in these analyses. Image analyses were performed by investigators blind to the animal genotypes and by automated Matlab scripts (minimal investigator-driven selection artifacts).

In vivo GCaMP imaging in barrel cortex. For awake Thy1-GCaMP6s4.3 experiments, both male and female mice at least 6 weeks of age were fitted with a chronic cranial window and implanted with a titanium headpost according to established procedures with minor alterations[39]. Briefly, animals were anesthetized with isoflurane (5% induction, 1.5–2% maintenance) and IP injected with a cocktail of dexamethasone (4 mg/kg), Rimadyl (carprofen 10 mg/kg), and Enroflox (enrofloxacin 5 mg/kg). Animals were mounted on a stereotaxic frame (David Kopf Instruments, Tujunga, CA) and body temperature was maintained with a thermal regulator (Harvard Apparatus, Holliston, MA). The scalp was shaved and sterilized with alternating swabs of Betadine and 70% alcohol. A small skin flap was removed, the periosteum was gently cleared, and the skull was scraped with a scalpel. A small circular craniotomy was made over the left barrel cortex (3-mm diameter; center relative to bregma: lateral 3.5 mm; posterior 1.8 mm) using a dental drill, and the dura was left intact. Two 3-mm glass coverslips were glued onto a 5-mm glass coverslip, and the cranial window was sealed by gluing these coverslips directly to the bone (VetBond, 3 M). The titanium headpost was implanted by adhering it directly to the bone using VetBond and then dental cement (Metabond, Parkell, Edgewood, NY). Animals recovered on a warm blanket before being placed back in their home cage. Rimadyl was injected (5 mg/kg) for 3 consecutive days after surgery for pain management. Following 1 week recovery from surgery, IOS imaging was performed through the cranial window, as described above, using light (0.5–1%) isoflurane anesthesia to locate principle whisker areas (typically the C2 whisker). The following week, animals were slowly habituated to headfixation with increasing time spent under headfixation, up to 1 h, which was continuously monitored via IR videography (Basler, acA640-120um). Mice were headfixed in

a custom-built stainless-steel body tube and mounting brackets. Noise associated with the resonant scanner was recorded and continuously played through speakers (Avisoft-UltraSoundGate, Avisoft Bioacoustics) within the microscope enclosure during habituation and imaging. Once mice were comfortable with headfixation (typically after 4 d), awake in vivo GCaMP imaging was performed. Mice were then injected with 0.5 MU of onabotulinumtoxinA (Botox, Allergan; prepared in PBS) into the right whisker pad under isoflurane anesthesia using a Hamilton syringe (2.5-μL 62 RN model, beveled tip), and allowed to recover for 2 d before repeating awake in vivo GCaMP imaging. Whisker paralysis, as demonstrated in Supplementary Video 2, lasted ~5 d.

For Gad2-T2A-NLS-mCherry × *Syngap1* mice (that is, Fig. 5) and Cre-driver mouse experiments (that is, Fig. 4), both male and female mice at least 6 weeks of age were fitted with a chronic cranial window and implanted with a titanium headpost according to the procedures detailed above. GCaMP6s was expressed following transduction with an rAAV (AAV1.Syn.GCaMP6s.WPRE. SV40, University of Pennsylvania Vector Core). During cranial window surgeries, iontophoresis via pulled-glass capillary micropipettes (Harvard Apparatus, Holliston, MA; 1.2-mm O.D., 0.69-mm I.D., inner tip diameter 20 μm) was used for infection at 4–6 sites within the craniotomy. Iontophoresis was performed with 5 μA at 7-s 'on' and 7-s 'off' cycles for 5 min total per injection site at a depth of ~200 μm. Following 2–3 weeks recovery from surgery, IOS imaging was performed as described above, using light (0.5–1%) isoflurane anesthesia, to locate principle whisker areas that overlapped with GCaMP6s expression (typically the C2 whisker). In vivo GCaMP imaging was performed ~4 weeks following surgery under light (1–1.5%) isoflurane anesthesia.

Imaging was performed with a VivoScope two-photon microscope equipped with a resonant scanner (Scientifica, UK). The light source was a Mai Tai HP 100 femtosecond-pulse laser (Spectra-Physics) running at 940 nm for GCaMP and 1,040 nm for mCherry imaging. The objective was a 16× water immersion lens with 0.8 NA (Nikon). Images were acquired using ScanImage 5 (http://vidriotechnologies.com). Functional images (512 × 512 pixels, 4× zoom, 150 × 150 μm) of L2/3 cells (70–250 μm below the pia) were collected at 10 Hz. Output at 100% laser power was 165 mW at the front aperture of the objective. For all GCaMP imaging experiments, we used 30–60% power, depending on the imaging depth. A similar number of imaging sessions at similar depths (~7 sessions starting at >70 μm below the pia in 30-μm intervals) were acquired for each animal.

Analysis of GCaMP activity in barrel cortex. Calcium images were corrected for motion artifacts using the moco plugin in ImageJ[58]. All subsequent analyses were performed in Matlab R2015b using the FluoroSNNAP15.04.08 plugin[59] with the following parameter choices. Regions of interest (ROIs) corresponding to identifiable cell bodies were selected manually. The fluorescence time course was measured by averaging all pixels within the ROI, then corrected for neuropil contamination. The neuropil ROIs were also manually drawn where there were no visible cell bodies and were the same for all cells within an imaging frame. After neuropil correction, the $\Delta F/F$ of each ROI was calculated as $(F - F_0)/F_0$, where F_0 was the mean of the lower 50% of the proceeding 10-s period. For the first 10-s period, a minimum value of F_0 was used[59]. A template search-based algorithm was used in order to detect calcium events using built-in templates in FluoroSNNAP15.04.08. A correlation coefficient of 0.8 and $\Delta F/F$ amplitude threshold of 15% was used during template search. Spontaneous activity was recorded over 2 min. Neurons with at least one detected calcium event during a 2-min period were classified as spontaneously active neurons. Whisker-stimulation-induced activity was also recoded over a 2-min period from the same ROIs. Whisker stimulation consisted of 5 whisker stimulations at 5 Hz or 60 whisker stimulations at 40 Hz, with an intertrain interval of 10 s with the same whisker stimulation parameters used in IOS imaging (~6°). Therefore, each single stimulus train lasted for 1 or 1.5 s. A total of 12 trains were given during a 2-min period. Raw response probability was calculated as the total number of calcium events during the 1-s or 1.5-s stimulation window divided by the total number of trains (12). To adjust for the probability of obtaining calcium events nonspecifically during the stimulation detection window, we subtracted the expected number of spontaneous calcium events from the raw calcium event count before dividing by 12. Cells with response probabilities greater than 0.083 (responding to 1 of 12 stimulations) were considered responders. For Gad2-T2A-NLS-mCherry × *Syngap1* experiments, mCherry fluorescence was recorded for 1 min. Images were flattened and merged onto GCaMP6s images to delineate inhibitory neurons from excitatory neurons. ROIs for excitatory and inhibitory neurons were analyzed in a fashion similar to that described above.

In vivo whole-cell recordings. A custom in vivo whole-cell patch-clamp system was built as described[60]. Mice were anesthetized with 1.6 g/kg urethane (Sigma-Aldrich, St. Louis, MO), followed by implantation of a custom headplate, and a 1-mm craniotomy was made over the barrel cortex. Recordings were performed the same day in current-clamp mode with the following internal solution in the electrode (mM): 130 potassium gluconate, 5 KCl, 10 HEPES, 10 sodium phosphocreatine, 0.4 EGTA, 1 Na-GTP and 4 Mg-ATP (pH 7.3, 285–290 mOsm). Electrophysiological signals were amplified with Multiclamp 700B (Molecular Devices, Sunnyville, CA), filtered at 2 kHz, digitized (10 KHz) with an NI USB-6363 (National Instruments,

Austin, TX), and recorded using the NI acquisition system in Matlab[61]. Up/down states were identified as described[29]. Briefly, the signal was first filtered with a median filter (100-ms window) to eliminate action potentials. Voltage segments lasting at least 100 ms and higher or lower than 1/3 s.d. away from the signal mean were classified as up or down states, respectively. To obtain synaptic currents, whiskers were deflected 5 times at 5 Hz with intensity parameters used during imaging experiments. To obtain synaptic amplitudes, 50 trials were averaged, excluding the trials with the action potentials. Action potentials were defined as samples where the speed of depolarization exceeded 6 mV/ms and whose values were more than 2 s.d. away from the mean.

Dendrite reconstructions: AAV systemic injections, tissue clearing, Sholl analysis. Dendrite reconstructions were performed in mice (*Syngap1* crossed to *Ai9*^{+/+}) that were injected with an rAAV9-packaged Cre-expressing virus via the superficial temporal vein (STV) at P1 as described previously[62]. Briefly, pups were sedated by covering them with ice for 3 min. STV was visualized using a handheld transilluminator (WeeSight; Respironics, Murrysville, PA, USA), and a pair of standard reading glasses. Virus solution was prepared by 1:50 dilution of stock solution in Dulbecco's phosphate-buffered saline (PBS), supplemented with 0.001% pluronic-F68. Virus solution (50 nL) was injected using a 100-nL Nanofil syringe attached to a 34-gauge Nanofil beveled needle (World Precision Instruments, Sarasota, FL). Correct injections were verified by noting blanching of the vein. After the injection, pups were returned to the incubator until active and then returned to their dam.

For dendritic tracing, P60 animals were deeply anesthetized with pentobarbital (Nembutal) and transcardially perfused with 4% PFA/PBS (wt/vol). Extracted brains were post fixed in 4% PFA/PBS at 4 °C for 10 h and cryoprotected in 20% sucrose/PBS (wt/vol) at 4 °C for 24 h. Brains were cut on a vibratome (500 μm thickness) collecting the somatosensory cortices. Slices were immediately submerged in Scale A2 solution in order to clear the tissue. When the tissue was transparent (at least 2 weeks), brain slices were mounted in Petri dishes, covered in agarose, and imaged using standard confocal microscopy. Three-dimensional image stacks were collected (*x*: 2,048, *y*: 2,048 pixels; step size: 1 μm) using confocal microscopy equipped with water immersion objective lens (ULTRA 25×, numerical aperture 1.05, Olympus). A computer-based tracing system (Neurolucida360; MicroBrightField) was used to generate three-dimensional neuron tracings that were subsequently visualized and analyzed with NeuroExplorer (MicroBrightField). To select a neuron, the following criteria were strictly followed: (i) a neuron was selected starting toward the middle of the stack (~150 μm ± 30 μm) to ensure the accurate reconstruction of an entire dendritic arbor; (ii) the neuron was distinct from other neurons to allow for identification of branches; and (iii) the neuron was not truncated in some obvious way. For every reconstructed neuron, an estimate of dendritic complexity within L2/3 and L4 neurons was obtained with Sholl analysis. A 3D Sholl analysis was then performed in which concentric spheres of increasing radii (20-μm increments) were layered around the cell body until branches were completely enveloped. The total length of branches, the number of dendritic intersections at each sphere, and the dendritic orders were measured[50]. Neurons were traced by an experimenter blind to genotype.

Spine density analysis. Because the tissue-clearing method enhanced the quality of our images, spine density was determined using the same set of images previously acquired for the tracing experiment. As previously described[50], ten to 15 dendritic segments of somatosensory cortex L2/3 and L4 (20–120 μm in length) were collected from P60 mice and considered for analysis. All measurements were performed by an experimenter blind to the experimental conditions. Pictures were visualized and elaborated with Neurolucida 360 software (MicroBrightField).

Acute slice preparation and in vitro electrophysiology. Acute thalamocortical (TC) slices (350 μm) from 8-week-old *Syngap1* WT and Het mice were cut using standard methods as previously described[63]. Ice-cold cutting solution contained (in mM): 110 choline-Cl, 25 NaHCO$_3$, 1.25 NaH$_2$PO$_4$, 2.5 KCl, 0.5 CaCl$_2$, 5 MgCl$_2$, 25 glucose, 10 ascorbic acid, 5 pyruvic acid (pH 7.4, ~300 mOsm). The slices were then warmed to 35 °C for 40 min in standard artificial cerebrospinal fluid (aCSF), composed of (mM): 125 NaCl, 2.5 KCl, 24 NaHCO$_3$, 2 CaCl$_2$, 1.25 NaH$_2$PO$_4$, 2 MgSO$_4$, and 10 D-glucose, and equilibrated with 95% O$_2$ and 5% CO$_2$ (pH 7.4, ~300 mOsm). Following this, slices were maintained in bubbled aCSF at room temperature (20–22 °C) until transferred to a submerged-type recording chamber (Warner Instruments, Hamden, CT). All experiments were performed at 32 °C ± 2 (2–3 mL/min).

Whole-cell patch-clamp experiments were conducted from visually identified L2/3 neurons using infrared DIC optics, and regular spiking was confirmed in current-clamp mode. Recordings were made using borosilicate glass pipettes (3–6 MΩ; 0.6-mm inner diameter; 1.2-mm outer diameter; Harvard Apparatus). All signals were amplified using Multiclamp 700B (Molecular Devices, Sunnyville, CA), filtered at 2 kHz, digitized (10 kHz), and stored on a personal computer for offline analysis. Analog to digital conversion was performed using the Digidata 1440 A system (Molecular Devices). Data acquisitions and analyses were performed using pClamp 10.2 software package (Clampex and Clampfit programs; Molecular Devices).

For current-clamp and evoked excitatory postsynaptic current (eEPSC) recordings, the following internal solution was used (in mM): 130 potassium gluconate, 5 KCl, 10 HEPES, 0.25 EGTA, 10 phosphocreatine disodium, 0.5 Na-GTP, and 4 Mg-ATP (pH 7.3, 285–290 mOsm). For miniature excitatory postsynaptic current (mEPSC) recordings, the following internal solution was used (in mM): 120 CsCl, 5 NaCl, 1 MgCl$_2$, 10 HEPES, 10 EGTA, 3 Mg-ATP, and 0.3 Na-GTP (pH 7.3, 285–290 mOsm). Cells with access resistance > 30 MΩ or that were unstable (>20% change) were discarded from further analysis.

In eEPSC experiments, slices were incubated with 100 µM picrotoxin. L4 was stimulated by placing a concentric bipolar stimulating electrode (FHC, 25-µm inner diameter; 125-µm outer diameter, ME, USA) in the center of a barrel. L2/3 neurons were recorded directly above the stimulus site. The stimulation intensity (0.2 ms, constant-current pulses) was regulated by a stimulus isolation unit (ISO-Flex, A.M.P.I.). A minimum-stimulus-intensity protocol was employed (6 sweeps with 15-s ISI) in current-clamp mode, as eEPSPs appeared to be more stable than eEPSCs recorded in voltage-clamp. The stimulus intensity was gradually increased until the emergence of an eEPSP with a 30–50% failure rate. This stimulus intensity was used in voltage-clamp mode to elicit eEPSCs from 15 sweeps (15-s ISI). eEPSCs were quantified by averaging the peak amplitudes, within a 30-ms post-stimulus window, excluding failures. Only one neuron was recorded from a single barrel column and a maximum of two neurons per slice. mEPSCs were recorded in TTX (1 µM), picrotoxin (100 µM), and APV (100 µM) at a holding potential of –75 mV. For each recording, the first 500 events were analyzed using Mini Analysis software (Synaptosoft Inc., NJ). Intrinsic properties of neurons were recorded at the resting membrane potential and measured as described[24].

Novel texture discrimination task (NoTeDt). Before testing for NoTeDt, mice were first habituated to an open field arena. Cohorts of mice were handled for several minutes on 3 separate days before commencement of behavioral testing. On the first day of the behavioral assay, mice were subjected to the open field habituation phase, during which an animal was allowed to explore a custom-made clear acrylic arena (43 cm × 43 cm × 32 cm tall) for two 10-min sessions per day, for 2 d. Opaque white acrylic dividers surrounded each arena to prevent distractions from activities in adjacent boxes. Activity was monitored with two CCTV cameras (Panasonic WV-BP334) feeding into a computer equipped with Ethovision XT 11.5 for data acquisition and analyses. A white-noise generator (2325-0144, San Diego Instruments) was set at 70 dB to mask external noises and provide a constant noise level. Fluorescent linear strip lights placed on each of the four walls of the behavioral room adjacent to the ceiling provided a lower-lighting (100 lx) environment. Distance traveled was analyzed as an indicator of familiarization to the experimental environment.

NoTeDt was performed in the same arenas used for open field habituation. The cylindrical objects were conceived to promote whisker-like explorations. Objects were designed by optimizing criteria from previously described and validated texture-based object discrimination tasks[64,65]. Briefly, white polyoxymethylene objects were 15 cm tall, fixed to a 5 cm diameter base, and the rough portion of the object covered 7.5 cm of the surface, starting 2 cm from its base. Two different grades of roughness (T1 and T2) were chosen and tested to determine whether the objects shared similar degree of attractiveness.

After the habituation phase (see open field section for details), mice were allowed to explore two identical objects (T1) for 10 min (learning phase). After 5 min, necessary for rearranging the arena (cleaning and replacing one of the objects T1 with the novel object T2), mice were exposed to the testing phase, in which they were allowed to explore both old and new objects. The location of the novel object was pseudorandomized and counterbalanced between groups. Time spent exploring textures was assessed by manually scoring each trial (offline), during both learning and testing phases. Mice that did not explore the objects during the learning phase, explored only one of the two objects during the testing phase, or had a total investigation time of less than 20 s during the learning phase were excluded from the study for lack of adequate exploratory activity. Behavioral scoring was performed by an experimenter blind to the experimental conditions.

Whisker-dependent go/no-go task. *Syngap1* WT and Het littermates (male, housed in a reverse light–dark room) were trained one session per day (~5 d/week) to perform a headfixed, whisker-dependent go/no-go task[39]. The behavioral apparatus was controlled by open-source BControl software (C. Brody, Princeton University) on an RT Linux machine[66]. A custom titanium headpost was implanted onto the skull at 6–10 weeks after birth. Briefly, animals were anesthetized with isoflurane (5% induction, 1.5–2% maintenance) and injected IP with Rimadyl (carprofen 10 mg/kg) and Enroflox (enrofloxacin 5 mg/kg). A small flap of skin was removed over the midline, and the skull was scraped with a scalpel before a thin layer of cyanoacrylate glue (Vetbond, 3 M) was applied. The headpost was implanted onto this layer of glue and secured with dental cement (Metabond). Animals were then singly housed and monitored for 1 week following surgery, with added environmental enrichment (running wheel). All behavioral sessions occurred during the dark phase. Weekly and throughout the experiment, all whiskers were trimmed to the base except for the C2 whisker on either side. Following recovery from headpost surgery, mice were placed on water restriction (1 mL/d) for 10 d before and then throughout training (food ad libitum). Water-restricted mice were monitored for health issues and weighed daily. On day six of water restriction,

habituation to headfixation commenced with increasing time spent under headfixation, up to 1 h. Mice were headfixed in a custom-built stainless-steel body tube, inside a fully enclosed light and soundproof box, which was continuously monitored via IR videography. On the last day of habituation, video recordings (30 FPS, Basler, acA640-120um) were obtained (45-min duration) under IR illumination to determine basic whisking properties (bouts and bout durations). Whisking was scored manually, offline (Solomon Coder) by an experimenter blinded to mouse genotypes.

Mice moved through a series of training steps. First, lick-port training (one session lasting 10 min) allowed mice to associate water availability via licking from a lick-port, with the C2 whisker inserted into a pipette (with ~2 mm at the base exposed) attached to a piezo actuator (Physik Instrumente), however, no passive whisker deflections were introduced. The metal lick-port was positioned directly in front of and slightly below the mouth, within reach of the tongue. Detection of licks was performed electronically[67] and precise water delivery (8 µL/reward) was controlled with a solenoid valve (The Lee Company, CT). Next, Step 1 training lasted for two sessions and represented the first time mice were exposed to passive whisker deflections. Here sessions consisted of 90% go and 10% no-go trials. For go trials, the whisker was deflected by the piezo actuator, controlled by a linear voltage amplifier (Physik Instrumente) and a waveform generator (BK Precision), for 1.5 s with a 40-Hz sinusoidal wave (rostral to caudal, 1,200 °/s). Bending of the piezo was calibrated using a laser-based displacement device (LD1610-0.5 Micro-Epsilon). For no-go trials, a 'dummy' piezo, placed just above the whisker-deflecting piezo, was driven with the same stimulation, but was not attached to a whisker. The response window was defined from 0.1 to 4 s after the start of piezo stimulation. For go trials, hits consisted of trials in which mice licked for a water reward within the response window, and misses were scored as lack of licking during this same period. For no-go trials, a false alarm (FA) resulted when the animal licked during the response window, and a correct rejection occurred when the animal withheld licking. No punishments were given for FAs and no auditory cue was presented. The intertrial interval remained constant at 4 s, but mice were required to withhold licking for 1.5 s before the piezo was stimulated for trials to proceed. Mice performed the task until satiated. Step 2 training was similar to Step 1, except sessions consisted of 50% go and 50% no-go trials (200–350 trials/session) with no more than three consecutive trials of the same type. The response window was shortened to 2 s. Training persisted until mice reached several performance criteria for at least 2 consecutive days: (i) overall performance reached >70% correct for all trials, (ii) hits > 70%, (iii) FAs < 30%, and (iv) discrimination index (d') > 1.1. d' was calculated in Excel (Microsoft) as $d' = z(hit) - z(FA)$, with z scores computed using the function NORMSINV. If mice did not reach criteria by 21 d, training was halted. 'Good performers' graduated to Step 3, in which the stimulus duration was reduced to 0.5 s. Mice continued this training until the same criteria was met as in Step 2. These mice graduated to a reduced stimulation protocol. Here sessions consisted of the same experimental setup as Step 3, except angular velocity of passive whisker deflections were reduced from 1,200 °/s to a range between 300 and 900 °/s.

Statistics. Data analyses were conducted in SPSS (IBM Corp, version 20), MATLAB (MathWorks, version 2015b, Natick, MA) and GraphPad Prism 7 (GraphPad Software, CA). D'Agostino–Pearson omnibus normality tests were applied to determine data distributions, and the appropriate parametric or nonparametric statistical test was performed accordingly. However, for experiments with small sample sizes ($n < 8$ subjects per group), statistical tests tend to lack the power to detect deviations from normality, and therefore a more subjective approach was used. For these cases, when data appeared to approximate a normal distribution, we assumed normality and used parametric statistical tests (that is, Figs. 5c and 8n, but not limited to these panels). For analysis of imaging data, the following tests were used: two-sided Student's t test was used to compare IOS amplitudes, IOS interbarrel distance, GWI-integrated $\Delta F/F$, GWI ratio of fourth/first pulse to first pulse, and the fraction of responding cells (except in Fig. 2d, where two-way RM-ANOVA was used) between genotypes; two-way RM-ANOVA was used to compare area measures for both relative and absolute thresholding methods for IOS and for peak responses and integrated $\Delta F/F$ in GWI experiments; Kolmogorov–Smirnov test was used to compare event amplitudes, event counts/2 min, and response probabilities, with Bonferroni-adjusted P values to control for type-I errors when multiple pairwise comparisons were made. For cluster analyses of spike counts, we pooled all spikes for each genotype and treatment, then performed a two-step cluster analysis. We specified a fixed number of (3) clusters for low-, medium- and highly-responsive neurons and used the Euclidean distance for computing the similarity between clusters. The numbers of neurons in each cluster were then separated into groups based on genotypes and treatment for further analysis. Differences in the clustered data were analyzed using chi-squared analysis. Pairwise post hoc comparisons between clusters and groups were performed using chi-squared analysis with Bonferroni-adjusted P values to control for type-I errors. For analysis of the neuronal morphology of L2/3 and L4 neurons, two-sided Student's t test, assessing the contribution of total length, number of nodes, and spine density were performed. For electrophysiology data, two-sided Student's t test, Mann–Whitney U test (when applicable), or Kolmogorov–Smirnov test was used to compare measurements between WT and Het mice. Two-way RM-ANOVA was used to compare

response amplitudes of responses to each whisker deflection and the number of spikes in response to current injections. NoTeDt behavioral data are expressed as the median ± interquartile except in Fig. 1b,e, where they are expressed as mean ± s.e.m. Nonparametric Friedman and Mann–Whitney U tests were used to analyze WT and Het performance in both learning and testing phases. Post hoc comparisons were performed using sign tests, and the Benjamini–Hochberg false discovery rate (FDR)-controlling procedure was used to compute the adjusted level of significance. One-sample t tests were performed against a chance value of 50% to determine whether the mice were able to discriminate between the novel and old textures. For go/no-go behavioral data, the following tests were used: two-way RM-ANOVA with Bonferroni's multiple comparisons post hoc test was used to compare performance (P(lick)) of WT and Het mice, performance with reduced angular velocity of whisker stimulation, normalized weights, number of trials performed, response times, and number of total licks; one-way RM-ANOVA with Bonferroni's multiple comparisons post hoc test was used to compare d' with reduced angular velocity of whisker stimulation; two-sided Student's t test or Mann–Whitney U tests were used to compare d' between WT and Het mice, mean water licks, total reward licks, mean trials/session, total trials performed, mean licks/trial (total), number of total licks, and basic whisking parameters; Fisher's exact test was used to compare proportion of performers vs. nonperformers in WT and Het mice. Unless otherwise stated, data represent mean ± s.e.m. No statistical test was used to predetermine sample sizes, but our sample sizes are similar to those previously reported in the field[68].

Reporting Summary. Further information on research design is available in the Nature Research Reporting Summary linked to this article.

Code availability. Custom code was written in Matlab to analyze intrinsic imaging experiments. Minor code modifications to the FluoroSNNAP15.04.08 plugin[59] were used to analyze somatic GCaMP6 signals. These scripts are available upon reasonable request.

Data availability

The data that support the findings of this study are available from the corresponding author upon reasonable request.

References

51. Kim, J. H., Lee, H. K., Takamiya, K. & Huganir, R. L. The role of synaptic GTPase-activating protein in neuronal development and synaptic plasticity. *J. Neurosci.* **23**, 1119–1124 (2003).
52. Harrison, T. C., Sigler, A. & Murphy, T. H. Simple and cost-effective hardware and software for functional brain mapping using intrinsic optical signal imaging. *J. Neurosci. Methods* **182**, 211–218 (2009).
53. Chen-Bee, C. H., Kwon, M. C., Masino, S. A. & Frostig, R. D. Areal extent quantification of functional representations using intrinsic signal optical imaging. *J. Neurosci. Methods* **68**, 27–37 (1996).
54. Chen-Bee, C. H. et al. Visualizing and quantifying evoked cortical activity assessed with intrinsic signal imaging. *J. Neurosci. Methods* **97**, 157–173 (2000).
55. Chen-Bee, C. H. & Frostig, R. D. Variability and interhemispheric asymmetry of single-whisker functional representations in rat barrel cortex. *J. Neurophysiol.* **76**, 884–894 (1996).
56. Goldey, G. J. et al. Removable cranial windows for long-term imaging in awake mice. *Nat. Protoc.* **9**, 2515–2538 (2014).
57. Holtmaat, A. et al. Imaging neocortical neurons through a chronic cranial window. *Cold Spring Harb. Protoc.* **2012**, 694–701 (2012).
58. Dubbs, A., Guevara, J. & Yuste, R. moco: fast motion correction for calcium imaging. *Front. Neuroinform.* **10**, 6 (2016).
59. Patel, T. P., Man, K., Firestein, B. L. & Meaney, D. F. Automated quantification of neuronal networks and single-cell calcium dynamics using calcium imaging. *J. Neurosci. Methods* **243**, 26–38 (2015).
60. Desai, N. S., Siegel, J. J., Taylor, W., Chitwood, R. A. & Johnston, D. Matlab-based automated patch-clamp system for awake behaving mice. *J. Neurophysiol.* **114**, 1331–1345 (2015).
61. Desai, N. S. & Walcott, E. C. Synaptic bombardment modulates muscarinic effects in forelimb motor cortex. *J. Neurosci.* **26**, 2215–2226 (2006).
62. Ozkan, E. D. et al. Input-specific regulation of hippocampal circuit maturation by non-muscle myosin IIB. *J. Neurochem.* **134**, 429–444 (2015).
63. Agmon, A. & Connors, B. W. Thalamocortical responses of mouse somatosensory (barrel) cortex in vitro. *Neuroscience* **41**, 365–379 (1991).
64. Heyser, C. J. & Chemero, A. Novel object exploration in mice: not all objects are created equal. *Behav. Processes* **89**, 232–238 (2012).
65. Wu, H. P., Ioffe, J. C., Iverson, M. M., Boon, J. M. & Dyck, R. H. Novel, whisker-dependent texture discrimination task for mice. *Behav. Brain Res.* **237**, 238–242 (2013).
66. Gaffield, M. A., Amat, S. B., Bito, H. & Christie, J. M. Chronic imaging of movement-related Purkinje cell calcium activity in awake behaving mice. *J. Neurophysiol.* **115**, 413–422 (2016).
67. Slotnick, B. A simple 2-transistor touch or lick detector circuit. *J. Exp. Anal. Behav.* **91**, 253–255 (2009).
68. He, C. X. et al. Tactile defensiveness and impaired adaptation of neuronal activity in the *Fmr1* knock-out mouse model of autism. *J. Neurosci.* **37**, 6475–6487 (2017).

naturesearch

Corresponding author(s):   Gavin Rumbaugh

Reporting Summary

Nature Research wishes to improve the reproducibility of the work that we publish. This form provides structure for consistency and transparency in reporting. For further information on Nature Research policies, see <u>Authors & Referees</u> and the <u>Editorial Policy Checklist</u>.

Statistical parameters

When statistical analyses are reported, confirm that the following items are present in the relevant location (e.g. figure legend, table legend, main text, or Methods section).

n/a	Confirmed	
☐	☒	The <u>exact sample size</u> (*n*) for each experimental group/condition, given as a discrete number and unit of measurement
☐	☒	An indication of whether measurements were taken from distinct samples or whether the same sample was measured repeatedly
☐	☒	The statistical test(s) used AND whether they are one- or two-sided *Only common tests should be described solely by name; describe more complex techniques in the Methods section.*
☐	☒	A description of all covariates tested
☐	☒	A description of any assumptions or corrections, such as tests of normality and adjustment for multiple comparisons
☐	☒	A full description of the statistics including <u>central tendency</u> (e.g. means) or other basic estimates (e.g. regression coefficient) AND <u>variation</u> (e.g. standard deviation) or associated <u>estimates of uncertainty</u> (e.g. confidence intervals)
☐	☒	For null hypothesis testing, the test statistic (e.g. *F*, *t*, *r*) with confidence intervals, effect sizes, degrees of freedom and *P* value noted *Give P values as exact values whenever suitable.*
☒	☐	For Bayesian analysis, information on the choice of priors and Markov chain Monte Carlo settings
☒	☐	For hierarchical and complex designs, identification of the appropriate level for tests and full reporting of outcomes
☒	☐	Estimates of effect sizes (e.g. Cohen's *d*, Pearson's *r*), indicating how they were calculated
☐	☒	Clearly defined error bars *State explicitly what error bars represent (e.g. SD, SE, CI)*

Our web collection on <u>statistics for biologists</u> may be useful.

Software and code

Policy information about <u>availability of computer code</u>

Data collection	The µManager plugin (Version 1.4) in ImageJ was used for IOS and GWI image acquisition. For in vivo GCaMP imaging, we acquired images using ScanImage 5.2 software, running on MATLAB (2013b). To replicate noise associated with the resonant scanner, Avisoft-Recorder (USGH 4.2.27) and Avisoft-SASLab Pro (5.2.12) software was used. For in vivo electrophysiology experiments, data was acquired by a custom in vivo whole cell patch clamp system, with a National Instruments acquisition system in MATLAB (2015b), as previously described (Desai et al., 2015). Neurolucida 360 (V.2017.01.1) was used to generate three-dimensional neuron tracings. For slice electrophysiology experiments, data was acquired using Clampex (10.2) software from the PCLAMP10 Software Suite (Molecular Devices). Ethovision XT (11.5) was used for the novel texture discrimination task. BControl software (C. Brody) running on MATLAB (2013a) was used to control the Go/NoGo apparatus.
Data analysis	Custom scripts written in MATLAB (2015b), as well as the IO and VSD Signal Processor (Version 1.0.8) plugin in ImagJ were used to analyze IOS and GWI imaging data, while cellular GCaMP imaging data was analyzed using FluoroSNNAP15.04.08 running on MATLAB (2015b). Motion artifacts were corrected with the moco plugin (03-18-2016) in ImageJ, while ImageJ (Version 1.50) was used to analyze Mcherry fluorescence. Visualization and analysis of three-dimensional neuron tracings was performed with NeuroExplorer (Version 4). For electrophysiology experiments, data was analyzed using Clampfit (10.2, Molecular Devices) software. Ethovision XT (11.5) was used for data analysis of the novel texture discrimination task. Basic whisking was scored manually, offline using Solomon Coder (17.03.22). Statistical analysis was performed in MATLAB (2015b), GraphPad Prism 7, Excel (16.14.1) and SPSS (Version 20).

For manuscripts utilizing custom algorithms or software that are central to the research but not yet described in published literature, software must be made available to editors/reviewers upon request. We strongly encourage code deposition in a community repository (e.g. GitHub). See the Nature Research <u>guidelines for submitting code & software</u> for further information.

Data

Policy information about availability of data

All manuscripts must include a data availability statement. This statement should provide the following information, where applicable:

- Accession codes, unique identifiers, or web links for publicly available datasets
- A list of figures that have associated raw data
- A description of any restrictions on data availability

> The data that support the findings of this study are available from the corresponding author upon reasonable request.

Field-specific reporting

Please select the best fit for your research. If you are not sure, read the appropriate sections before making your selection.

☒ Life sciences   ☐ Behavioural & social sciences   ☐ Ecological, evolutionary & environmental sciences

For a reference copy of the document with all sections, see nature.com/authors/policies/ReportingSummary-flat.pdf

Life sciences study design

All studies must disclose on these points even when the disclosure is negative.

Sample size	No statistical methods were used for determining sample sizes. However, our sample sizes are similar to those previously reported in the field (He et al., 2017,).
Data exclusions	Exclusion criteria for experimental data points were pre-determined as follows. Animal death during anesthetized experiments or deterioration of cranial window clarity during imaging experiments (limited to < 5% of cases), as reliable data acquisition could not be verified under these conditions. For neuronal morphology studies, only neurons with the following criteria were selected for tracing: 1) neuron was selected starting toward the middle of the stack (~150 µm ± 30 µm) to ensure the accurate reconstruction of an entire dendritic arbor; 2) neuron was distinct from other neurons to allow for identification of branches; 3) neuron was not truncated in some obvious way. For in vitro whole-cell patch clamp experiments cells with access resistance >30 MΩ or were unstable (>20 % change) were discarded from further analysis. For texture discrimination testing, mice that did not explore objects during the learning phase, explored only one of the two objects during the testing phase, or had a total investigation time of less than 20 s during the learning phase, were excluded from the study for lack of adequate exploratory activity.
Replication	We attempted to replicate data whenever possible by using multiple cohorts of animals (typically two), for imaging and behavior experiments. Results were reliably reproduced in these cases. We are encouraged by the fact that the cellular sensory properties in response to passive whisker stimulations in our imaging studies were repeatable in multiple mouse lines tested, including the Thy1-GCaMP6s4.3 x Syngap1, EMX1-Cre x Syngap1 cKO and Gad2-NLS-mCherry x Syngap1 lines. Furthermore, the resulting reduced neural responsiveness to passive whisker stimuli in awake Botox-treated (non-whisking) Thy1-GCaMP6s4.3 x Syngap1 animals was similar to those from the EMX1-Cre x Syngap1 cKO line under anesthesia, suggesting a repeatable phenotype across experimental conditions (ie. brain state). Our results from the Go/NoGo task were repeatable in our lab as this data was pooled from two separate cohorts that were conducted by two independent experimenters.
Randomization	Generation of multiple transgenic mouse lines was labor, time and resource intensive. Additionally, most experiments required 1-3 months to complete, even with small sample sizes. This prevented us from picking WT and Het animals randomly from litters. Therefore, to obtain comparable sample sizes between genotypes, animal cohorts were generated by allocating relatively equal number of age-matched Syngap1 WT and Het littermates from separate litters, usually more than two. Then, animals were assigned a number to hide identity of genotype and/or group assignment. For imaging and behavior tasks, animals were recorded once per day in a randomized order while blinded to genotype. For imaging experiments, stimulations were presented in a pseudo-random sequence for each imaging depth.
Blinding	For all studies, experimenters were blinded to genotype at the time of data acquisition and analysis.

Reporting for specific materials, systems and methods

Materials & experimental systems

n/a	Involved in the study
☒	☐ Unique biological materials
☒	☐ Antibodies
☒	☐ Eukaryotic cell lines
☒	☐ Palaeontology
☐	☒ Animals and other organisms
☐	☒ Human research participants

Methods

n/a	Involved in the study
☒	☐ ChIP-seq
☒	☐ Flow cytometry
☒	☐ MRI-based neuroimaging

Animals and other organisms

Policy information about studies involving animals; ARRIVE guidelines recommended for reporting animal research

Laboratory animals	The conventional and conditional Syngap1+/- mouse lines have been previously described (Kim et al., 2003, Clement at al., 2012) and maintained on a BL6/B129sv/ev hybrid genetic background. Thy1-GCaMP6s4.3 (#024275), Emx1-Cre (#05628), Gad2-NLS-mCherry (#023140), and the TdTomato Ai9 (#007905) reporter mouse lines were purchased from Jackson Laboratories and maintained on a pure C57BL/6J background. Rbp4-Cre (037128-UCD) and Cux2-CreERT2 (032779-MU) mouse lines were purchased from MMRC and maintained on a pure C57BL/6J background. Both males and females were used in all experiments indiscriminately, except for the Go/NoGo task, where only males were used. Data collection occurred from mice >8 weeks of age.
Wild animals	The study did not involve any wild animals.
Field-collected samples	The study did no involve any field-collected animals.

Human research participants

Policy information about studies involving human research participants

Population characteristics	The SYNGAP1 patient population was self-identified in the Registry. There were no entrance exclusions and anyone could join, upload medical records, medical data and answer questionnaires. Because of this, it was crucial to focus on patients in the sensory survey that included conclusive genetic information (i.e. a genetic report from a medical geneticist). These patients can be found in Supplementary Table 2.
Recruitment	Participants (parents or guardians) volunteered and provided informed consent prior to depositing medical data into the registry. There were no entrance exclusions and anyone could join, upload medical records, medical data, and answer questionnaires. Because of this, it was crucial to focus on patients in the registry that included conclusive genetic information (i.e. a genetic report from a medical geneticist). These patients can be found in Supplementary Table 2.